Master's Thesis

# IEEE 802.15.4a-UWB compliant Positioning using Energy Detectors

Johannes Benjamin Till

---

Signal Processing and Speech Communication Laboratory
Graz University of Technology
Head: Univ.-Prof. DI Dr. techn. Gernot Kubin


Supervisor/Assessor: DI Dr. Assoc.Prof. Klaus Witrisal
Supervisor: DI Thomas Gigl

Graz, May 2010

# STATUTORY DECLARATION

I declare that I have authored this thesis independently, that I have not used other than the declared sources / resources, and that I have explicitly marked all material which has been quoted either literally or by content from the used sources.

..... .....

Date NAME

# Abstract

In this thesis a step-by-step approach to positioning in IEEE 802.15.4a with the intention of reaching an accuracy of one meter is presented. The standard uses pulses with high bandwidth, which makes it suitable for high precision ranging and positioning through receiver-sided delay measurements. This thesis leads through all the steps needed for localization, beginning with signal acquisition, followed by ranging where two ranging algorithms are presented, and finally positioning where the developed algorithm are used in a real life tracking system. A graphical user interface is implemented that serves as real-time feedback device by presenting the user the positioning results. The obtained results satisfy the IEEE 802.15.4a standard's aim of providing a system with ranging and positioning accuracy in the sub-meter scale.

# Kurzfassung

In der vorliegenden Diplomarbeit wird eine schrittweise Herangehensweise an Positionierung präsentiert. Der hierzu verwendete IEEE 802.15.4a Standard wurde unter anderem mit dem Ziel entwickelt Lokalisierung mit einer Genauigkeit von rund einem Meter zu erreichen. Dazu werden ultrakurze Pulse verwendet, die es ermöglichen mithilfe von empfängerseitigen Signallaufzeitmessungen eine sehr genaue räumliche Auflösung zu erreichen. Diese Arbeit führt durch alle Schritte die notwendig sind in einem praktischen System Lokalisierung zu betreiben, beginnend mit der Signaldetektion, über Rangingalgorithmen, bishin zu Positionierung. Die theoretisch erarbeiteten Algorithmen wurden dazu verwendet in einem praktischen Laboraufbau Lokalisierung betreiben zu können. Die erzielten Ergebnisse tragen dem erklärten Ziel des IEEE 802.15.4a Standards hinsichtlich Genauigkeit genüge.

# Acknowledgements

I would like to take the opportunity to thank the people who made this work possible. I want to thank especially my supervisors Thomas Gigl and Klaus Witrisal, who helped me a lot and without whom this work would not have been possible. Furthermore a big thank goes to my mentor Erich Leitgeb, Bernhard Geiger, Katharina Hausmair and of course to my entire family who supported me throughout the way. Thank you all.

# Contents

# Chapter 1

# Introduction

Positioning and ranging have always been interesting and challenging topics of research. With the introduction of ultra-wideband (UWB) radio applications in the early 1990s a new candidate for this context has been found. UWB is defined by having either a relative bandwidth larger than 20% of the center frequency or an absolute bandwith of more than 500MHz [GTG+05]. Impulse-radio ultra-wideband (IR-UWB) uses very short pulses for transmission, enabling a high temporal resolution, which makes it suitable for high accuracy ranging and positioning applications in indoor and outdoor scenarios with a high accuracy through receiver sided delay measurements of the used pulses.

## 1.1 Motivation

While the techniques and algorithms for indoor and outdoor positioning are mostly the same, radio signals from already established outdoor systems like the global navigation satellite system (GPS/GNSS) suffer from a high attenuation when penetrating through walls and therefore perform poorly indoors. With Assisted-GPS/GNSS a new technique was developed using both weak satellite received data as well as localization information via mobile phone data link. Other possibilities are using an optical system like a laser tracker or localization with the help of ultrasound beacons [Mau09].

Radio frequency (RF) based approaches can be subdivided into angle-of-arrival (AOA) systems, where the angles between reference nodes are used to estimate position, received signal strength (RSS) systems, where the signal attenuation is exploited, and time based techniques where signal delay is measured. Time based approaches include the time-of-arrival (TOA) and time-difference-of-arrival (TDOA) methods.

The IEEE 802.15.4a standard implements a definition for a UWB-IR signal scheme

that uses pulses in the sub-nanosecond scale, offering sub-meter accuracy for positioning. Due to the high bandwidth of the pulses, the standard ensures that at least some of the different frequency components reach the receiver either by going through or around obstacles [GTG+05]. Due the short duration of the pulses, they offer the possibility of resolving multipath components. The high bandwidth also allows the signal energy to be spread over a wide range reducing the power spectral density and therefore allowing spectrum overlay with existing radio services.

## 1.2 Outline

Within this thesis a step by step approach to positioning is presented. Chapter 2 introduces the IEEE 802.15.4a signal scheme and its frame format. Chapter 3 deals with acquisition of the UWB-frame and Chapter 4 describes the proposed ranging algorithms. The algorithms will be compared with respect to their ranging capabilities and in their mathematical complexity. Chapter 5 gives an introduction to TDOA positioning and also includes an experimental setup of a tracking system and presents the achieved results for positioning. The work closes with conclusions and an outlook of future work and the Appendix where the measurement setup is described in detail for the interested reader.

# Chapter 2

# IEEE 802.15.4a

The IEEE 802.15.4a standard was defined by the IEEE 802.15 Low Rate Alternative PHY Task Group for Personal Area Networks (WPANs) as an amendment to the IEEE 802.15.4 standard with the intention of providing high precision ranging capability as well as ultra low power consumption and was approved as a new amendment in spring of 2008. The goal for the localization context is to provide accuracy in the scale of one meter or better.

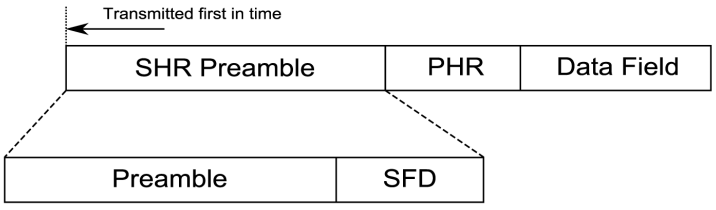


Figure 2.1: Structure of an IEEE802.15.4a transmission packet [Buc08].

## 2.1 Packet Structure

The standard defines an UWB frame that consists of two parts [IEE07]. The one sent first in time is the synchronization header (SHR), which only uses binary phase-shift keying (BPSK) as coding scheme. The SHR can further be subdivided into the preamble sequence and the start of frame delimiter (SFD). The SHR is followed by the information part of the transmitted packet that consists of the physical header (PHR) and the payload in the data field. The PHR contains information about the parameters used for transmission and is followed by the data field. The structure of an IEEE 802.15.4a transmission packet is illustrated in Figure 2.1. Both PHR and data use BPSK as well as burst position

modulation (BPM) to encode symbols, enabling the use of both coherent and non-coherent receivers. However, in this work only the SHR part of the packet is used for ranging and therefore only this portion is further detailed. All symbols are built up of ternary preamble sequences (TPS), which are discussed in the following subsection.

| Index | Code sequence |
|---|---|
| $\mathbf{C}_1$ | - 0 0 0 0 + 0 - 0 + + + 0 + - 0 0 0 + - + + + 0 0 - + 0 - 0 0 |
| $\mathbf{C}_2$ | 0 + 0 + - 0 + 0 + 0 0 0 - + + 0 - + - - - 0 0 + 0 0 + + 0 0 0 |
| $\mathbf{C}_3$ | - + 0 + + 0 0 0 - + - + + 0 0 + + 0 + 0 0 - 0 0 0 0 - 0 + 0 - |
| $\mathbf{C}_4$ | 0 0 0 0 + - 0 0 - 0 0 - + + + + 0 + - + 0 0 0 + 0 - 0 + + 0 - |
| $\mathbf{C}_5$ | - 0 + - 0 0 + + + - + 0 0 0 - + 0 + + + 0 - 0 + 0 0 0 0 - 0 0 |
| $\mathbf{C}_6$ | + + 0 0 + 0 0 - - - + - 0 + + - 0 0 0 + 0 + 0 - + 0 + 0 0 0 0 |
| $\mathbf{C}_7$ | + 0 0 0 0 + - 0 + 0 + 0 0 + 0 0 0 + 0 + + - - - 0 - + 0 0 - + |
| $\mathbf{C}_8$ | 0 + 0 0 - 0 - 0 + + 0 0 0 0 - - + 0 0 - + 0 + + - + + 0 + 0 0 |

Table 2.1: Length 31 ternary codes.

## 2.2 SHR

The symbols of the SHR preamble are constructed out of a predefined sequence of code symbols drawn from a ternary alphabet {-1,0,1}. The standard defines a variety of those spread codes with a fixed length $N_{code}$ of either 31 or 127 sub-symbols, which are called chips. The length-31 tables are depicted in Table 2.1. The codes for $N_{code} = 127$ are not illustrated in this work, but can be looked up in the standard [IEE07]. The ternary sequences have the property that the periodic autocorrelation function observed by coherent and non-coherent receivers is perfect, meaning the side lobes of the autocorrelation function are zero and what is observed in between peaks is the power delay profile (PDP) of the channel [SG06].

The UWB pulses used for transmission are modulated according to the TPS, where in case of {1,-1} the pulses' polarity is modulated and {0} means no pulse is sent. After pulse modulation, the code sequence $\mathbf{C}_i$ is spread by the delta function $\delta_L$ of length $L$. This is described mathematically in (2.1), where $\otimes$ is the Kronecker product.

$$\mathbf{S}_i = \mathbf{C_i} \otimes \delta_L[n] \tag{2.1}$$

$$\delta_L[n] = \begin{cases} 1 & n = 0 \\ 0 & 1, \ldots, L-1 \end{cases}$$

Figure 2.2 provides an overview of the spreading operation where $L-1$ zeros are inserted between the ternary elements of $\mathbf{C}_i$. Valid spreading factors $L$ for length 31 TPSs are 16 and 64, whereas for the long sequences only a spreading factor of 4 is intended by the standard. The total number of chips per symbol $N_c$ is given by

$$N_c = N_{code} L \tag{2.2}$$

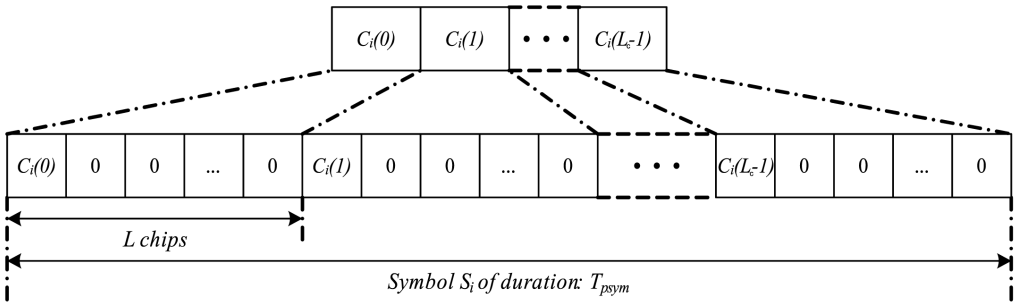


Figure 2.2: Construction of symbol $\mathbf{S}_i$ from code $\mathbf{C}_i$[IEE07].

### 2.2.1 SYNC Preamble

The SYNC part of the preamble, which is sent at the beginning of every transmission can be used for packet synchronization, channel estimation and ranging. The previously constructed symbols are repeated $N_{sync}$ times with $N_{sync} \in \{16, 64, 1024, 4096\}$. This allows four different possible durations $T_{sync}$ for the SYNC portion. Mathematically the repetition operation can be expressed as:

$$\mathbf{N}_i = \delta_N[n] \otimes \mathbf{S}_i \tag{2.3}$$

$$\delta_N[n] = \begin{cases} 1 & n = 0, \ldots, N_{sync} - 1 \\ 0 & elsewhere \end{cases} \tag{2.4}$$

When choosing a preamble length, one has to consider the higher processing gain that comes with the long and medium length SYNC portion but also the higher processing complexity. The signal during the SYNC part can be described as a waveform $p_i(t)$ by

$$p_i(t) = \sum_{n=0}^{N_c N_{sync}-1} \mathbf{N}_i[n] p(t - nT_c) \tag{2.5}$$

where $p(t)$ is the ultrashort pulse defined within the IEEE 802.15.4a standard.

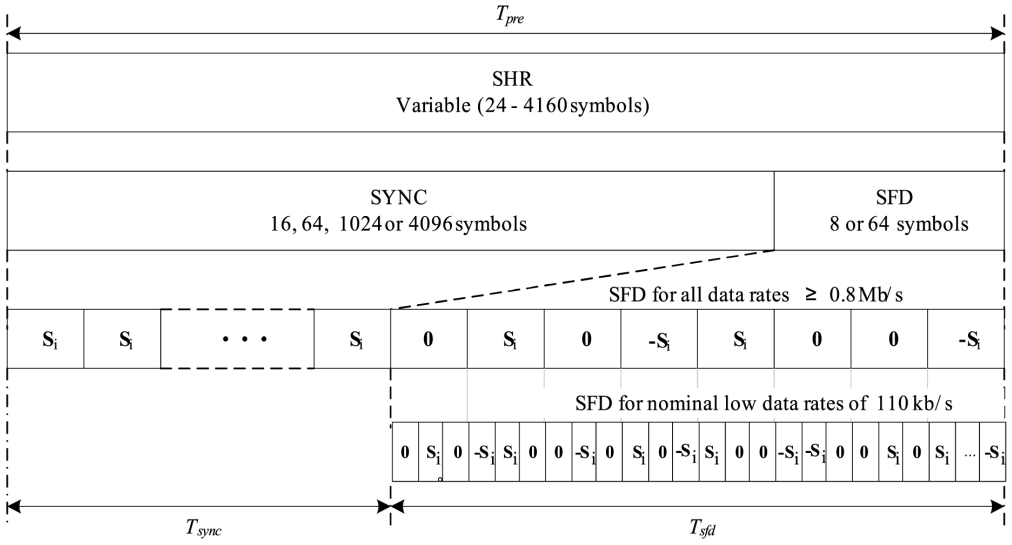


Figure 2.3: Detailed SHR preamble structure [IEE07](©IEEE 2007).

### 2.2.2 Start of Frame Delimiter

The SYNC portion is followed by the SFD that consists of $N_{sfd}$ preamble symbols $\mathbf{S}_i$ with $N_{sfd} \in$ (8,64), modulated by the sequence $\mathbf{A}$. The SFD is used for marking the end of the preamble sequence. The two possible sequences are shown in Table 2.2 and are denoted $\mathbf{A}_l$ for the long and $\mathbf{A}_s$ for the short option.

From the table it can be seen that only half of the symbols for $\mathbf{A}$ are active, so only half of the symbols actually contain energy because of the zero modulation parameter. Again, the spreading process can be described as the Kronecker product of the modulation parameter $\mathbf{A}$ with $\mathbf{S}_i$. The SFD waveform $z_i(t)$ is described in (2.7).

$$\mathbf{M}_i = \mathbf{A} \otimes \mathbf{S}_i \tag{2.6}$$

$$z_i(t) = \sum_{m=0}^{N_c N_{sfd}-1} \mathbf{A}_i[m] p(t - mT_c) \tag{2.7}$$

The first 16 symbols of the long SFD sequence $\mathbf{A}_l$ are just repetitions of the short one. This can be used to distinguish between short and long SFD without the need of running

| Index | Code sequence |
|---|---|
| $\mathbf{A}_l$ | 0 + 0 - + 0 0 - 0 + 0 - + 0 0 - - 0 0 + 0 - 0 + 0 + 0 0 0 - 0 - 0 - 0 0 + 0 - - 0 - + 0 0 0 0 + + 0 0 - - - + - + + 0 0 0 0 + + |
| $\mathbf{A}_s$ | 0 + 0 - + 0 0 - |

Table 2.2: SFD sequences.

two correlators, because the long one delivers two peaks when correlated against the short template. In addition to that, it is notable that $\mathbf{A}_s$ is a balanced sequence, ensuring zero output when the correlator slides through the transition between SYNC and SFD [SG06].

The overall signal sent during SHR is described by

$$x_i(t) = p_i(t) + z_i(t - N_{sync}T_{psym}) \tag{2.8}$$

where $T_{psym}$ is the duration of the spread preamble symbol given by

$$T_{psym} = N_{code}LT_c \tag{2.9}$$

### 2.2.3 UWB Pulse and Peak Repetition Frequency

The fundamental elements of the impulse radio part of the IEEE 802.15.4a standard are its UWB pulses. The four different pulse durations $T_p$ defined are 2.00, 0.92, 0.75 and 0.74ns. The pulses are sent at the so called peak pulse repetition frequency (PRF), where the reciprocal value $\frac{1}{PRF}$ is the duration of a single chip $T_c$ [Buc08]. The PRF is defined by the standard to be 499.2MHz.

# Chapter 3

# Signal Acquisition

## 3.1 Problem Statement

The acquisition part of the used algorithm has the challenge of determining whether a signal is present or not. The signal is always embedded in noise. If no signal is transmitted, only noise arrives at the receiver. The receiver has to process the incoming signal and decide among those two possibilities. This Chapter will (briefly) describe the receiver structure, the decision process that relies on a threshold detection, and the computation of the threshold itself.

## 3.2 Energy Detection

The signal $z_i(t)$ is sent over a channel with channel impulse response $h_c(t)$, so the received signal $r(t)$ becomes

$$r(t) = z_i(t) * h_c(t) + n(t) \tag{3.1}$$

where $n(t)$ is additive zero mean white Gaussian noise (WGN) and $*$ denotes the convolution. Figure 3.1 shows the used receiver architecture, which is implemented as an energy detector (ED). The ED is characterized by its low complexity and has the advantage that sub Nyquist sampling is possible. It consists of a bandpass filter to select the desired frequencies, a square law device and an integrator that sums up over an interval of $T_{int}$. The output of the integrator is then fed to a sampling device. The filter used is a so-called matched filter (MF) with an impulse response $p_f(t)$ that is proportional to

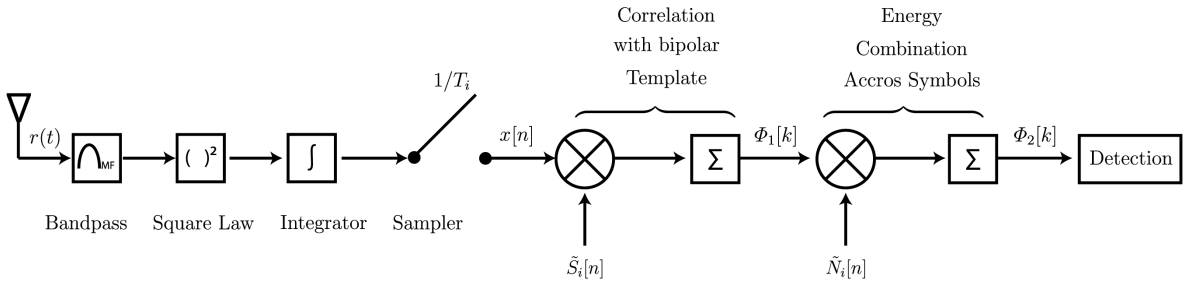


Figure 3.1: Overview over the detection process

$p(-t)$, the reversed copy of the transmitted pulse. The output of the MF becomes

$$r_f(t) = r(t) * p_f(t) \tag{3.2}$$

which is then squared and integrated over a period of $T_{int}$ and sampled, so that the output of the ED is

$$x[n] = \int_{nT_{int}}^{(n+1)T_{int}} r_f(t)\, dt \tag{3.3}$$

The integrated samples are further passed to a two step replica correlator for code despreading. In the first step the received signal is correlated with the known deterministic ternary preamble sequence. However all zero chips are set to -1 and all -1 are set to $+1$ in order to keep the perfect autocorrelation property of the chip code [Cea05]. The matched sequence is referred to as $\tilde{\mathbf{C}}_i$. Mathematically the matching process has the form $\tilde{\mathbf{C}}_i = 2|\mathbf{C}_i| - 1$ with $\mathbf{C}_i$ being the well known, not yet spread, TPS. This has to be done, because the ED is not able to determine the pulse polarity due to the square law device, so regardless if the received pulse was positive or negative, the ED always sees a positive one. Therefore, the used correlation sequence is now referred to as bipolar [Buc08].

The bipolar sequence is, according to [Cea05], the optimal template for detecting a ternary template using non-coherent receivers. It has to be spread according to (3.4) before cross-correlation, described in (3.5), can be performed.

$$\tilde{\mathbf{S}}_i = \tilde{\mathbf{C}}_\mathbf{i} \otimes \delta_L[n] \tag{3.4}$$

$$\Phi_1[k] = \sum_{n=0}^{k+(N_c-1)} x[n+k]\tilde{S}_i[n] \tag{3.5}$$

The peaks in $\Phi_1[k]$ correspond to the start of the particular preamble symbols. Having obtained their positions, energy combination across the symbols is performed by the second correlation process, where the output of the first is correlated with the known modulation parameters of the preamble symbols $\tilde{\mathbf{N}}_i$ that are given by (3.6), where $\delta_{N_c}$ is the delta function of length $N_c$ and $\mathrm{J}_{1,N_{sync}}$ is a vector of ones namely $[11\ldots1]_{1\times N_{sync}}$.

$$\tilde{\mathbf{N}}_i = \mathrm{J}_{1,N_{sync}} \otimes \delta_{N_c}[n] \tag{3.6}$$

This leads to a pyramid shaped function $\Phi_2[k]$, described in (3.7).

$$\Phi_2[k] = \sum_{n=0}^{k+(N_{sync}N_c)-1} \Phi_1[n+k]\tilde{N}_i[n] \tag{3.7}$$

The process of the two-step correlation is illustrated in Figure 3.1. The outcome of $\Phi_2[k]$ can now be compared with a threshold $\gamma$, and the detector decides that a signal is present when $\Phi_2[k] > \gamma$. The derivation of this threshold is described in the following section.

## 3.3 Threshold for Deterministic Signals

The problem of finding a descent threshold $\gamma$ is solved by using the Neyman-Pearson (NP) theorem, which is based on hypothesis testing. For a known signal embedded in Gaussian noise, two hypotheses have to be developed. $\mathcal{H}_0$ is the "noise only" case, and therefore the so called null hypothesis, and $\mathcal{H}_1$ is the case when signal and noise are present, the alternative hypothesis [Kay93]:

$$\begin{aligned} \mathcal{H}_0 : x[n] &= w[n] \\ \mathcal{H}_1 : x[n] &= s[n] + w[n] \end{aligned} \tag{3.8}$$

In the equation above $w[n]$ is zero mean WGN with known variance $\sigma^2$ and $s[n]$ is the signal. The probability density functions (PDF) under each hypothesis will have differences in means, causing the PDF under $\mathcal{H}_1$ to be shifted to the right due to the present signal [Kay93]. The PDFs for null and alternative hypothesis are depicted in

Figure 3.2. Now, the detector has to decide $\mathcal{H}_1$ if $x[n] > \gamma$, with $\gamma$ being threshold derived from the noise characteristics and the deterministic signal.

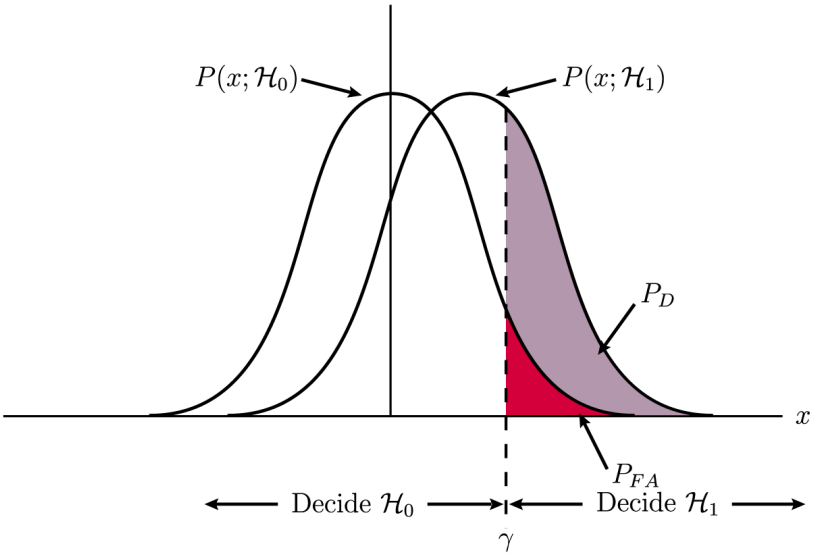


Figure 3.2: PDFs for hypothesis testing and decisions regions and probabilities [Kay93].

There are two different errors that might occur when working with hypothesis testing: The likelihood that the detector decides $\mathcal{H}_1$ when $\mathcal{H}_0$ is true or in other notation $P(\mathcal{H}_1;\mathcal{H}_0)$ is referred to as the probability of false alarm ($P_{FA}$). The other error probability is $P(\mathcal{H}_0;\mathcal{H}_1)$. $P(\mathcal{H}_1;\mathcal{H}_1)$ is called the probability of detection ($P_D$). The $P_{FA}$ should be rather small to avoid false detection. However, it is not possible to reduce both error probabilities at the same time [Kay93]. When setting the $P_{FA}$ to a very small value the $P_D$ will decrease as well. The typical approach is to set the $P_{FA}$ to a fixed constraint while minimizing $P(\mathcal{H}_0;\mathcal{H}_1)$ and therefore maximizing the $P_D$.

The NP detector decides $\mathcal{H}_1$ if the likelihood ratio $L(x)$ exceeds $\gamma$ (3.9).

$$L(x) = \frac{P(x;\mathcal{H}_1)}{P(x;\mathcal{H}_0)} > \gamma \tag{3.9}$$

According to [Kay93], the detection performance $T(x)$ for a given $P_{FA}$ can be determined using the replica correlator form

$$T(x) = \sum_{n=0}^{N-1} x[n]s[n] > \gamma \tag{3.10}$$

Under each of the two hypotheses, $T(x)$ will have a Gaussian distribution if $x[n]$ is also distributed Gaussian. However, using an ED neither $\mathcal{H}_0$ nor $\mathcal{H}_1$ will be distributed that way, but a Gaussian approximation can be made under certain circumstances which

will be discussed in Subsection 3.4.1. For now, $x[n]$ is considered to be Gaussian, hence $T(x)$ is the linear combination of random variables of such a kind of distribution, and therefore Gaussian itself.

$E(T;\mathcal{H}_i)$ and $\mathrm{var}(T;\mathcal{H}_i)$ denotes the expected value and variance of $T(x)$ under $\mathcal{H}_i$. The following equations show the variance for the test statistics $T(x)$ in the "no signal" case to be the product of the noise variance and the energy $\varepsilon$ of the used replica with

$$\varepsilon = \sum_{n=0}^{N-1} s^2[n] \tag{3.11}$$

The expected values of T in the noise-only and signal-and-noise case are described by (3.12) and (3.13) respectively [Kay93]. That yields the variance for the noise only case in (3.16), which is needed to derive the desired threshold.

$$\begin{aligned}
E(T;\mathcal{H}_0) &= E\left(\sum_{n=0}^{N-1} w[n]s[n]\right) = 0 && (3.12)\\
E(T;\mathcal{H}_1) &= E\left(\sum_{n=0}^{N-1} (s[n]+w[n])s[n]\right) = \varepsilon && (3.13)\\
\mathrm{var}(T;\mathcal{H}_0) &= \mathrm{var}\left(\sum_{n=0}^{N-1} (s[n]+w[n])s[n]\right) && (3.14)\\
&= \left(\sum_{n=0}^{N-1} \mathrm{var}(w[n])s^2[n]\right) && (3.15)\\
&= \sigma^2 \sum_{n=0}^{N-1} s^2[n] = \sigma^2\varepsilon && (3.16)
\end{aligned}$$

The test statistic becomes

$$T \sim \begin{cases} \mathcal{N}(0,\sigma^2\varepsilon) & \text{under } \mathcal{H}_0 \\ \mathcal{N}(\epsilon,\sigma^2\varepsilon) & \text{under } \mathcal{H}_1 \end{cases} \tag{3.17}$$

with $\mathcal{N}(\mu,\sigma^2)$ denoting a Gaussian PDF with mean $\mu$ and variance $\sigma^2$. Following [Kay93], $P_{FA}$ and $P_D$ can be computed using the right-tail probability $Q(\gamma)$ and its inverse function $Q^{-1}(P_{FA})$. The latter gives a threshold for a desired $P_{FA}$ and the first delivers the probability that a random variable will obtain a value larger than $\gamma$. So finally the $P_D$ can be expressed as [Kay93]

$$\begin{aligned} P_D &= Q\left(\frac{\sqrt{\sigma^2\varepsilon}Q^{-1}(P_{FA})}{\sqrt{\sigma^2\epsilon}} - \sqrt{\frac{\varepsilon}{\sigma^2}}\right) \\ &= Q\left(Q^{-1}(P_{FA}) - \sqrt{\frac{\varepsilon}{\sigma^2}}\right) \end{aligned} \tag{3.18}$$

leading to the finding of the threshold with [Kay93]

$$\gamma = \sqrt{\sigma^2\varepsilon}Q^{-1}(P_{FA}) \tag{3.19}$$

where $\varepsilon$ is the energy of the used replica and $\gamma$ is the threshold that maximizes the $P_D$ for a given $P_{FA}$.

## 3.4 Adjusted Threshold for UWB-TPS

In the previous Section it was shown that the process of correlating the incoming signal with its known replica leads to test statistics with different mean values causing a shift to the right for $P(T;\mathcal{H}_1)$. This is valid for a deterministic signal of zero mean. But in fact the sequences of the used ternary code are not zero mean, as well as the modulation parameter used to perform the second correlation. This causes the two PDFs to be further shifted to the right and has to be considered in the equation used to compute the threshold. As shown before, the threshold can be computed as described in (3.19). For better illustration there are two thresholds $\gamma'$ and $\gamma''$ listed below. The first one can be used for detection after the first correlation on preamble symbol level $\Phi_1[k]$ whereas $\gamma''$ can be used at the output of the second correlator on combined symbol level. In this work only detection on combined symbol level is performed so the first threshold is purely for derivation explanation.

Substituting $s[n]$ with the used spread TPS $S_i[n]$ leads to Equation (3.20)

$$\gamma' = Q^{-1}(P_{FA})\sqrt{\sigma^2 \sum_{n=0}^{N_c-1} \tilde{S}_i^2[n]} \tag{3.20}$$

When detection is performed after the second correlator, $\gamma''$ must be used that also takes the modulation parameters in $\tilde{\mathbf{N}}_i$ into account:

$$\gamma'' = Q^{-1}(P_{FA})\sqrt{\sigma^2 \sum_{n=0}^{N_c-1} \tilde{S}_i^2[n] \sum_{n=0}^{(N_{sync}N_c)-1} \tilde{N}_i^2[n]} \tag{3.21}$$

Without correction, the non zero mean properties of $\mathbf{S}_i$ and $\mathbf{N}_i$ lead to thresholds too low for the outcome of the test statistics, because the PDFs are shifted to the right by multiplying the mean $\mu$ of $x[n]$ by the sum of the used replicas $\tilde{\mathbf{S}}_i$ and $\tilde{\mathbf{N}}_i$, resulting in:

$$\gamma' = Q^{-1}(P_{FA})\sqrt{\sigma^2 \sum_{n=0}^{N_c-1} \tilde{S}_i^2[n]} + \mu \sum_{n=0}^{N_c-1} \tilde{S}_i[n] \tag{3.22}$$

and

$$\gamma'' = Q^{-1}(P_{FA})\sqrt{\sigma^2 \sum_{n=0}^{N_c-1} \tilde{S}_i^2[n] \sum_{n=0}^{(N_{sync}N_c)-1} \tilde{N}_i^2[n]} + \mu \sum_{n=0}^{N_c-1} \tilde{S}_i[n] \sum_{n=0}^{(N_{sync}N_c)-1} \tilde{N}_i[n] \tag{3.23}$$

Substituting the sums in (3.22) and (3.23) with $\varepsilon_{TPS}$ and $\varepsilon_{sync}$ for

$$\varepsilon_{TPS} = \sum_{n=0}^{N_c-1} \tilde{S}_i^2[n] \tag{3.24}$$

$$\varepsilon_{sync} = \sum_{n=0}^{N_c-1} \tilde{S}_i^2[n] \sum_{n=0}^{(N_{sync}N_c)-1} \tilde{N}_i^2[n] = \varepsilon_{TPS} \sum_{n=0}^{N_{sync}N_c-1} \tilde{N}_i^2[n] \tag{3.25}$$

leads to the terms for the thresholds $\gamma'$ and $\gamma''$

$$\gamma' = Q^{-1}(P_{FA})\sqrt{\sigma^2 \varepsilon_{TPS}} + \mu \sum_{n=0}^{N_c-1} \tilde{S}_i[n] \tag{3.26}$$

$$\gamma'' = Q^{-1}(P_{FA})\sqrt{\sigma^2 \varepsilon_{sync}} + \mu \sum_{n=0}^{N_c-1} \tilde{S}_i[n] \sum_{n=0}^{(N_{sync}N_c)-1} \tilde{N}_i[n] \tag{3.27}$$

## 3.5 Gaussian Approximation

Due to the fact that an ED is used, the noise PDF is depending on the integration time not Gaussian after the integrator and sampler. It has a chi-square distribution in the absence of a signal and a noncentral chi-square distribution in the case that the signal is present [Urk67]. However, the output of the first correlator can be viewed as the sum of $M = N_c$, and the output of the second as sum of $M = N_{sync}N_c$ independent random

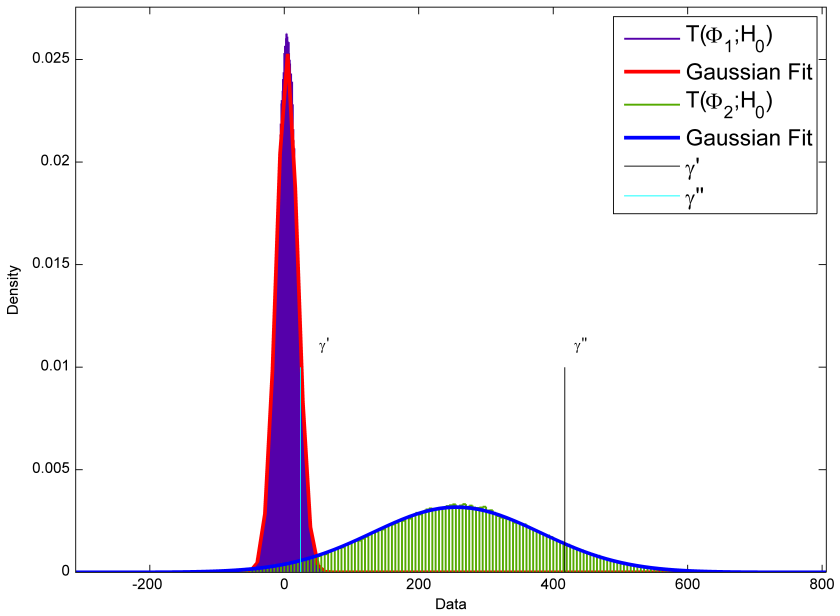


Figure 3.3: Test statistics under null hypothesis ($P_{FA} = 0.1$) for $\Phi_1$ and $\Phi_2$

variables. The resulting decision variable $T$ tends to be Gaussian according to the central limit theorem when $M$ tends to infinity. According to [DDdRO05], the Kolmogorov-Smirnov test - a method used to determine whether two sets of values are from the same continuous distribution - shows that when $M$ becomes higher than 40, the PDF of $T$ becomes Gaussian with a confidence higher than 5%. Since only $\gamma''$ is used for detection purposes, near Gaussian distribution for the test statistics of the second correlator can be assumed [DDdRO05]. Figure 3.3 shows the outcome of the test statistics for the correlation processes $\Phi_1$ and $\Phi_2$ under the null hypotheses, the calculated thresholds $\gamma'$ and $\gamma''$, as well as the fitted Gaussian distribution.

## 3.6 Simulation

The probability of successfully detecting the start of the SYNC portion is investigated for different energy-per-symbol-to-spectral-noise-density ratios $E_s/N_0$ by Monte Carlo simulations. In these simulations the $E_s/N_0$ is used to generate Gaussian noise, which is added to the signal after convolving the ternary data sequence with a set of channel impulse responses measured during a field campaign at the Speech Communication and Signal Processing Laboratory (SPSC) and different other locations [GBG+09]. The start

of the signal is shifted to simulate different arrival times within the integration period $T_{int}$ [Gei09b]. The overall process is depicted in Figure 3.1. As described in Chapter 2 the SHR is made up of $N_{sync} + N_{sfd}$ repetitions of a ternary code sequence that contains $N_c$ chips. The detection works on combined symbol level, using the SYNC portion of the transmitted signal. The $P_{FA}$ is set to $10^{-8}$, and the integration time is varied from 2 to 32 ns with $T_{int} \in \{2, 4, 8, 16, 32\}$ns. These borders have been chosen because the latter is the duration length $L$ of the used delta function $\delta_L[n]$ in (2.1), and the shortest integration period is equivalent to the used pulse duration $T_P$.

### 3.6.1 Detection

Another parameter that is varied is the number of preamble symbols across which energy combination is performed. Using less symbols results in fewer mathematical operations at the second correlator. The outcome of the second correlator (see Figure 3.5), as described in Equation 3.7, has $N_{red} - 1$ increasing peaks spaced by $T_{psym}$ before the comb of the correlation template is located perfectly across the preamble symbols, leading to the maximum peak of the pyramid shaped function. $N_{red}$ denotes the reduced number of SYNC symbols to correlate with. Peaks located at

$$k = k_{start} - jT_{psym} \text{ with } j \in \{1, \dots N_{red} - 2\} \tag{3.28}$$

are also considered as valid detection points, with $k_{start}$ denoting the moment when the correlation pattern is located perfectly across the signal, thus resulting in the highest peak at $\Phi_2[k_{start}]$. The time period where a detection event is rated to be correct is set to 8ns for all integration durations beginning at the start of each of the peaks described in (3.28). Detection events outside that time period are considered to be false alarm events. This is done to establish a common constraint for all possible $T_{int}$s. The output of the second and first correlator are exemplarily illustrated in Figures 3.4 and 3.5.

The highest peak in Figure 3.5 is assumed to be the starting point of the preamble sequence. In the transitions phase, where the correlator slides through the window, the correlation fits the sequence better and better until perfect overlap. Figure 3.6 shows the augmented area around this peak with marked the sample $k_{start}$ as well as the area of valid detection for that peak.

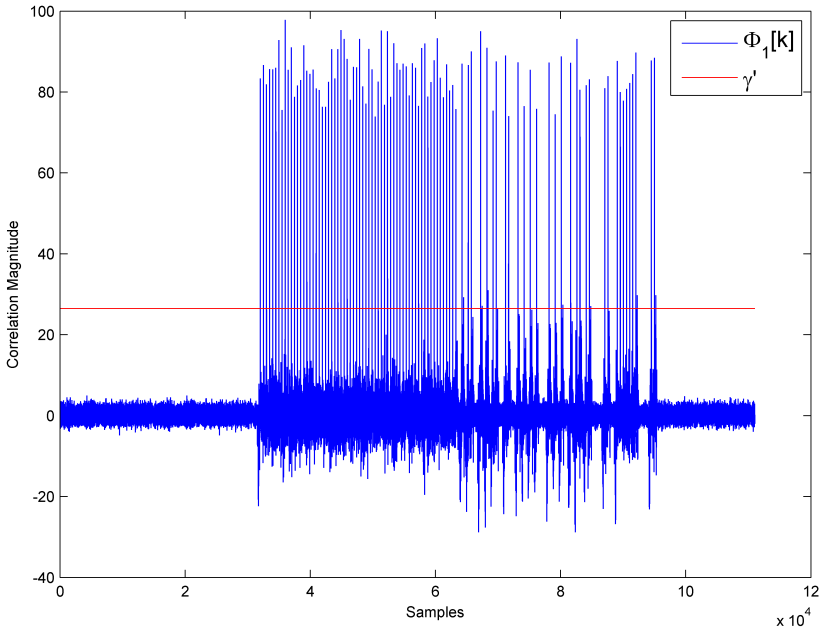


Figure 3.4: Output of the first correlator

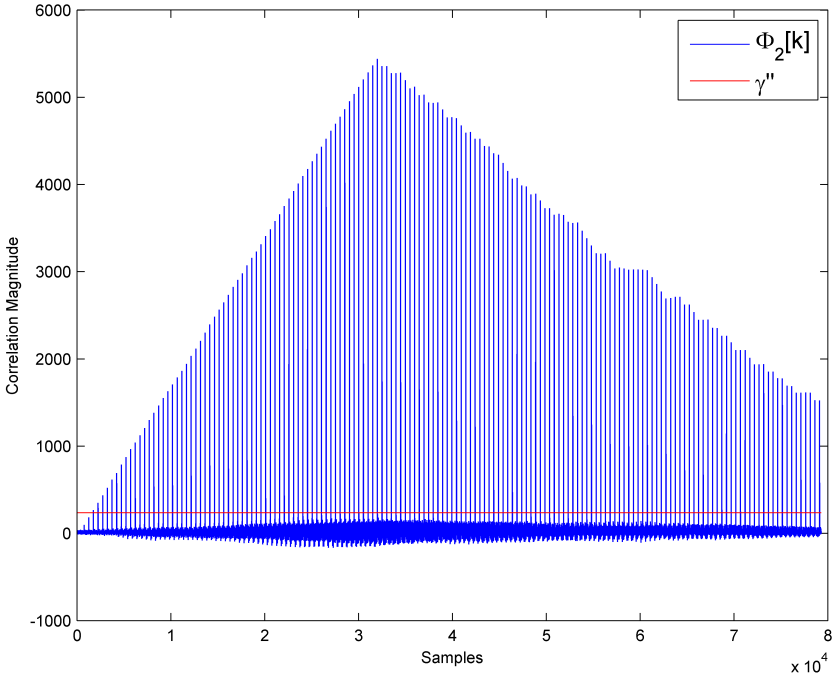


Figure 3.5: Output of the second correlator

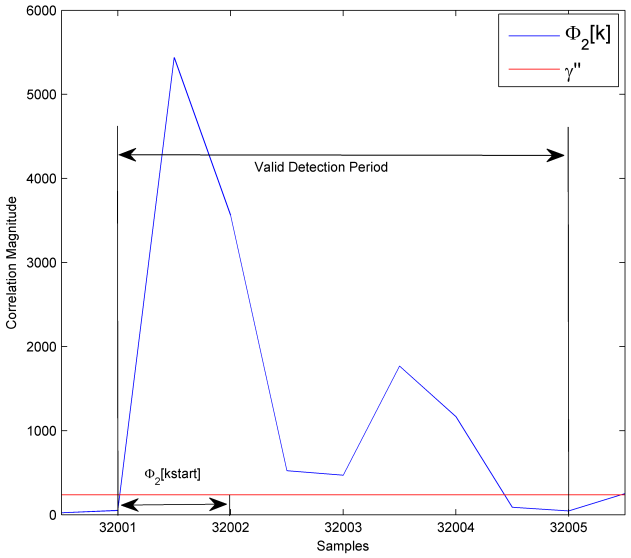


Figure 3.6: Zoom in on highest peak from Figure 3.5 at $T_{int} = 2$ns.

### 3.6.2 Simulation Results

In Figure 3.7 the probability of correct detection is plotted against the signal-to-noise ratio. Different curves for different $N_{red}$ show an increasing chance of correct detection when combining more preamble symbols to trigger the detection process. This is due an higher processing gain achieved by increasing $N_{red}$. The performance is also assessed by measuring the probability of SYNC acquisition for extended integration intervals $T_{int}$, in order to reduce the length of the signal that has to be processed, also resulting in lower complexity and less mathematical operations. It can be shown that for a longer $T_{int}$ not only more signal energy is collected, but also more noise samples, which results in a decreasing probability of correct acquisition [WLJ+09]. This is due to the threshold that is derived from the noise characteristics of the integrated signal. When changing the integration period duration, the changing variance causes a different threshold and then the noise energy is more likely to outmatch the signal energy the longer the integration period becomes, causing the detector to decide that no signal is present when in fact there is. From the results it can be seen that the probability of detection decreases by approximately one dB for each step of doubling the integration time. The spacings among the curves of constant $T_{int}$ thereby stays the same. This shows that a doubling of the preamble symbols results in a 1.5dB gain in terms of robustness. Investigating the detection process for more than $N_{sync}$=64 has not been done, because as shown in the next Chapter, the limiting factor for ranging operations is the SFD which is used as

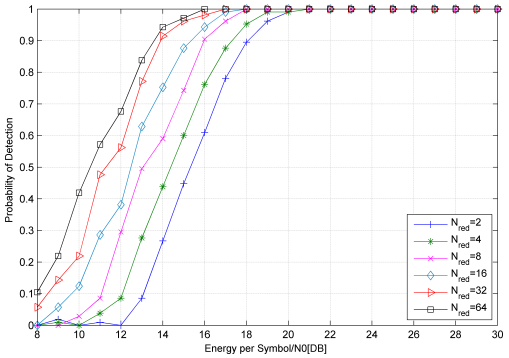


(a) $T_{int}$=2ns.

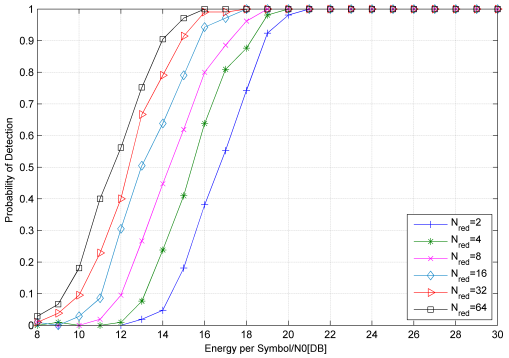


(b) $T_{int}$=4ns.

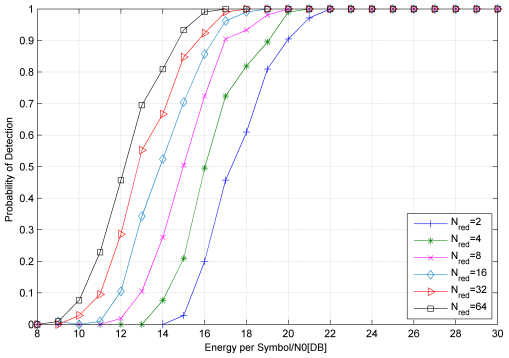


(c) $T_{int}$=8ns.

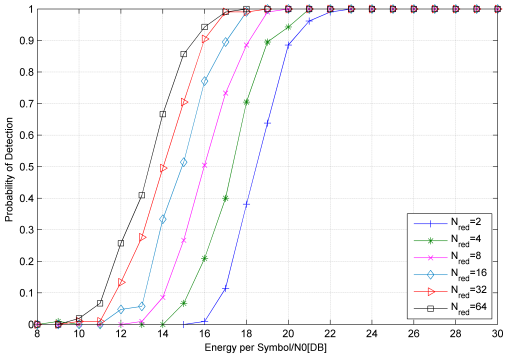


(d) $T_{int}$=16ns.

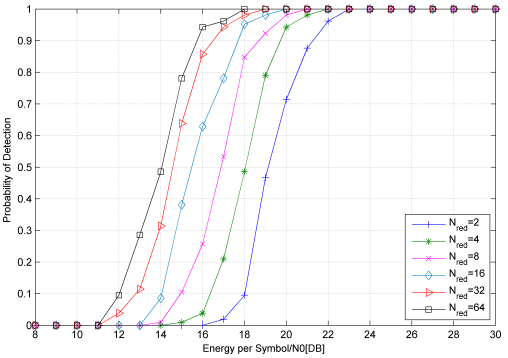


(e) $T_{int}$=32s.

Figure 3.7: Acquisition results for different $T_{int}$.

ranging marker.

# Chapter 4

# Ranging

## 4.1 Overview

Having achieved synchronization, as shown in the previous Chapter, the focus in this Chapter is the implementation and comparison of two ranging algorithms (RA) with the objective of determining the exact time-of-arrival (TOA) of the transmitted signal. The first RA applies the ranging process directly on the SFD after signal detection, while the second one will exploit the properties of the TPS as well as using information from detection process in order to reduce the total number of operations needed to achieve ranging. The two RAs will be analyzed in detail with respect to their ranging capabilities. Furthermore a complexity analysis will be presented.

## 4.2 Ranging Algorithm I

The first ranging algorithm is depicted in Figure 4.1. It shows the already known detection part while is extended by a second path, where the incoming signal is correlated against the bipolar sequence, producing $\Phi_{21}[k]$, which is then energy combined by correlating with the SFDs symbol sequence, resulting in $\Phi_{22}[k]$. The algorithm uses the fact that when the SFD is correlated with its replica, the output becomes one main peak with minor side lobes. This is because the symbols are nearly balanced, so the main lobe can easily be identified. Figure 4.2 shows a correlation of the received signal with the known SFD sequence with one major peak and minor side lobes during the transition phase.

The decision whether a frame is present or not is made by the detection process described in the previous Chapter. It triggers the ranging algorithm as soon as the

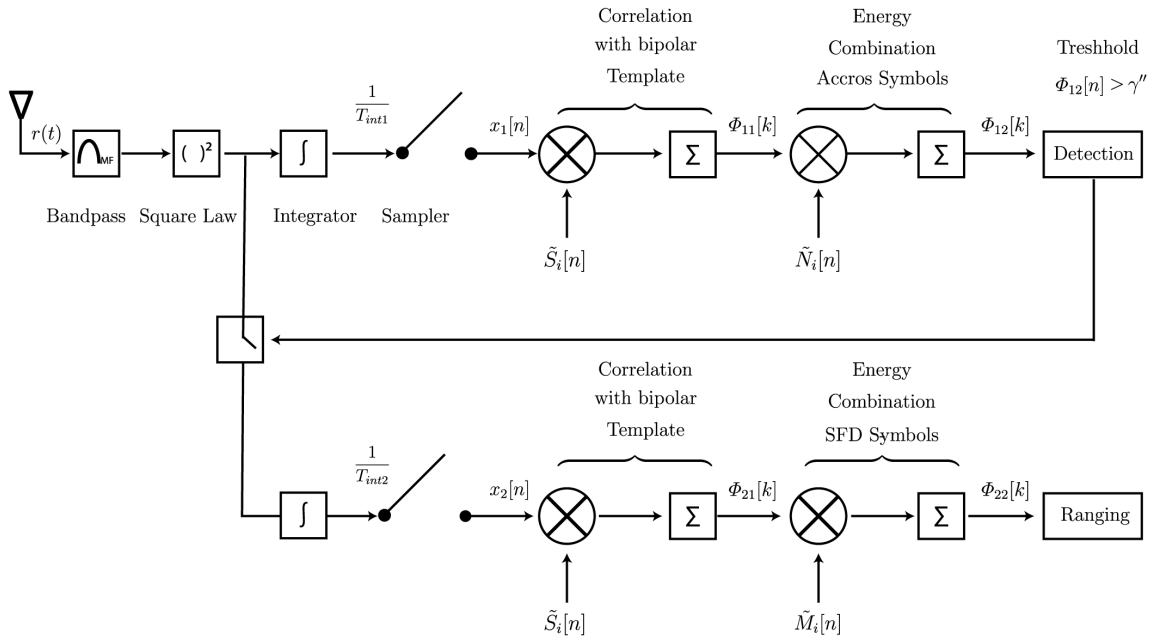


Figure 4.1: Ranging Algorithm I.

accumulated energy exceeds the given threshold.

After successful signal detection, which works at integration time $T_{int1}$ to save complexity, a switch is triggered that causes a second integrator that works at integration time $T_{int2} = T_p$ to sum up the incoming signal. Its output is then fed into the already known bipolar correlator given in (3.6) producing the output $\Phi_{21}[k]$. In difference to the detection process, energy combination is performed across the SFD symbols instead of those from the SYNC portion, leading to a single peak that can easily be identified by a simple maximum search to avoid the introduction of another threshold. The output of the SFD correlation process is depicted in Figure 4.2.

In the first part of the simulations different combinations of system parameters will be used to establish a well defined base under which conclusions can be drawn concerning reasonable system parameters for both detection and ranging part. However, in the second part, like proposed in [DMT09], the detection problem is ignored and the frame's presence is assumed to be detected successfully.

Mathematically the ranging part can be described as the correlation of the SFD symbol sequence with the output of (3.5)

$$\Phi_{22}[k] = \sum_{n=0}^{k+(N_{sfd}N_c)-1} \Phi_{21}[n+k]\tilde{M}_i[n] \tag{4.1}$$

with

$$\tilde{\mathbf{M}}_i = \tilde{\mathbf{A}}_\mathbf{i} \otimes \delta_{N_c}[n] \tag{4.2}$$

and

$$\tilde{\mathbf{A}}_\mathbf{i} = 2\,|\mathbf{A_i}| - 1 \tag{4.3}$$

In $\Phi_{22}[k]$ the highest peak is assumed to be the start of the SFD part. The detection of the line-of-sight component of the received signal within $\Phi_{22}[k]$ is discussed in the following section.

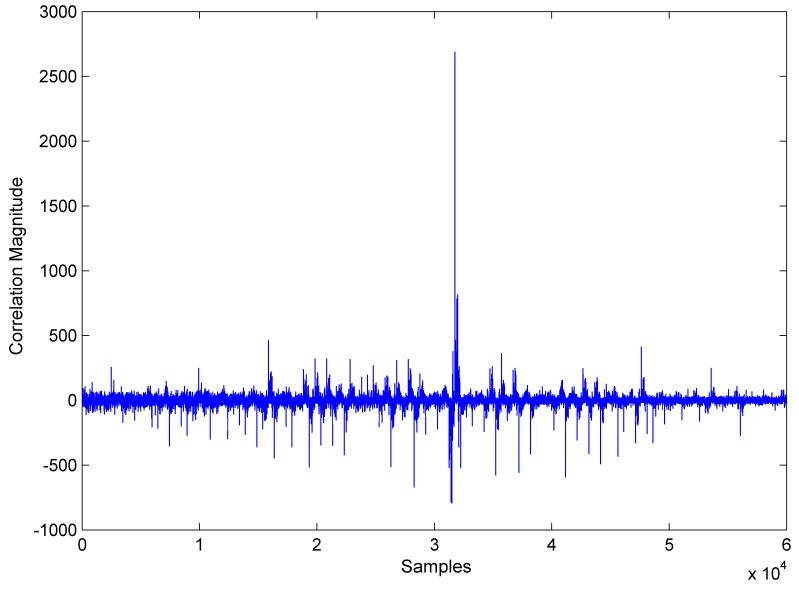


Figure 4.2: Output of the SFD template correlator.

### 4.2.1 Leading Edge Detection

Based on the energy combination across the SFD symbols by the second correlator, the highest peak can be identified. This peak corresponds to the signal from the strongest path, but since the strongest multipath component might not be the first impinging at the receiver, leading edge detection has to be implemented to find the exact TOA. This is done by using a search back-window (SB). Once presence of the signal has been discovered by the detector and the ranging marker has been found, a search-back algorithm is

performed within a predefined interval. The farthest point from the peak point exceeding the threshold $\gamma_{LE}$ can be considered the leading edge. Again, the threshold for the leading edge $\gamma_{LE}$ is closely related to the noise characteristics and can be computed following [GPPAW09] as

$$\gamma_{LE} = \overline{\nu}_{\Phi} + c(\Phi_{max} - \overline{\nu}_{\Phi}) \tag{4.4}$$

resulting in peak detection for $c = 1$ and in smaller threshold for $c \leq 1$. Here $\overline{\nu}_{\Phi}$ is the mean magnitude of the noise samples and is given by (4.5) and $\sigma^2_{\Phi}$ is the variance of $\Phi$ [GPPAW09].

$$\overline{\nu}_{\Phi} = \sqrt{\frac{\pi}{4}\sigma^2_{\Phi}} \tag{4.5}$$

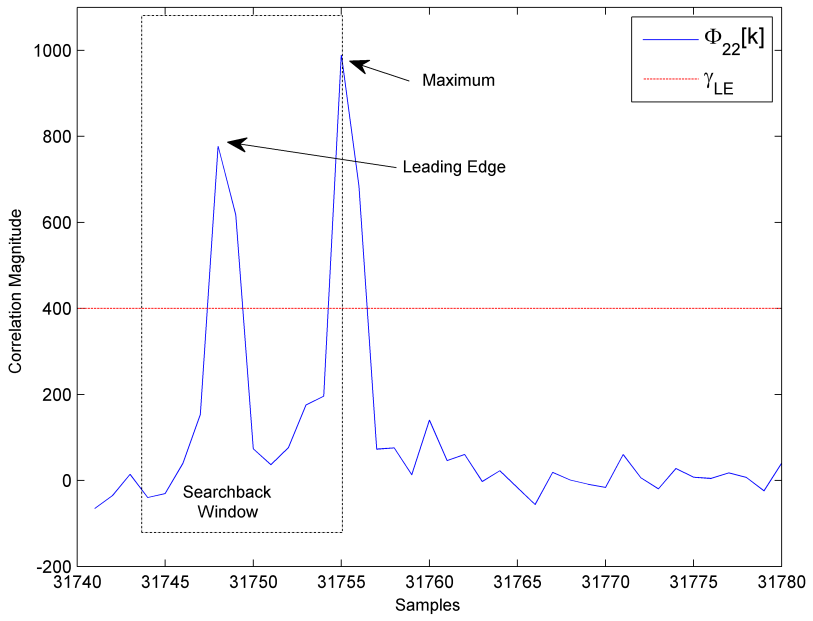


Figure 4.3: Leading edge detection

Using the maximum $P_{max}$ of the function $\Phi_{22}[k]$ as starting point - given in Equation 4.6 - the first or earliest sample within the fixed length of the SB interval exceeding $\gamma_{LE}$ is used as an estimate for the TOA.

$$P_{max} = \max_{k} \ \Phi_{22}[k] \tag{4.6}$$

The corresponding index of the sample where $P_{max}$ is located is

$$k_{max} = \arg\max_{k} \ \Phi_{22}[k] \tag{4.7}$$

The following equation delivers the index of the sample that resembles the estimated TOA:

$$k_{toa} = \arg\min_{k} \{k|\Phi_{22}[k] > \gamma_{LE}\} \Big|_{(k_{max}-w_{sb}) \leq k \leq k_{max}} \tag{4.8}$$

where $w_{sb}$ denotes the length of the search back window in samples.

### 4.2.2 Simulation Results

Since the mathematical computations for detection and ranging are the same, with the only difference being the part of the signal that is used, not all possible parameter combinations that the standard defines are reasonable. Using 1024 symbol repetitions for the SYNC portion may deliver a high possible processing gain concerning SNR for the detection part of the system, but when it comes to ranging with the symbols of the SFD, a successful identification at the same noise level might not be possible anymore, resulting in a global ranging error that is only limited by the length of the window used to find the maximum (4.6). Therefore, an equitable ratio of SYNC and SFD symbol repetitions has to be found. One has to keep in mind that even though the SFD is either 8 or 64 symbol durations $T_{psym}$ long, half of the symbols are zero in each case, and therefore don't contribute to the energy accumulation performed by the cross correlation processing. In order to establish a relation between detection and ranging processes, the simulations are conducted in the following way: Different integration periods $T_{int1}$ and quantities of symbols to be combined in order to trigger detection have been chosen, as well as the two SFD lengths resulting in a variety of combinations for the composite signal. Like in the previous simulations for the detection part, the integration duration $T_{int1} \in \{2, 4, 8, 16, 32\}$ns and $N_{red} \in \{2, \ldots N_{sync}\}$. The number of SFD symbols is set to 8 and 64, respectively, in accordance with the standard. Again the time period that was considered to be valid for the detection of the TOA is set to 8ns. The results depicted in Figures 4.4 and 4.5 show the probability of positively identifying the SFD under the condition that the acquisition process has ended successfully for the parameters varied as explained before.

What can be seen from the results, is that, caused by the lowered probability of detection for longer integration periods, the chance of finding the SFD for the use as ranging marker suffers as well. The second important thing that can be observed, is that the successful outcome of the overall process is mostly limited by the ability of correctly finding the maximum of the second correlation that resembles the beginning of the SFD and not by the detection process. With decreasing SNR, the likelihood of

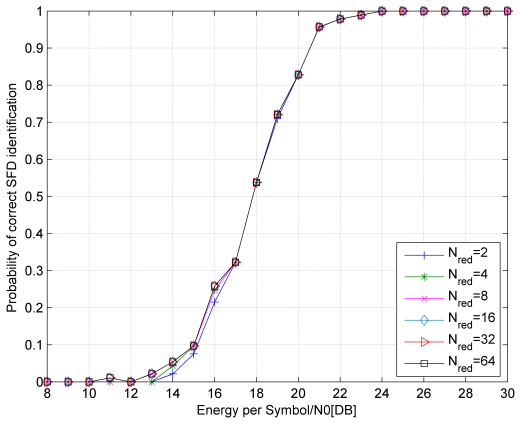


(a) $T_{int1}$=2ns.

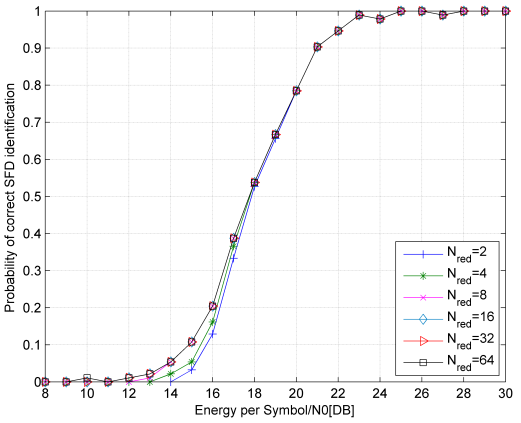


(b) $T_{int1}$=4ns.

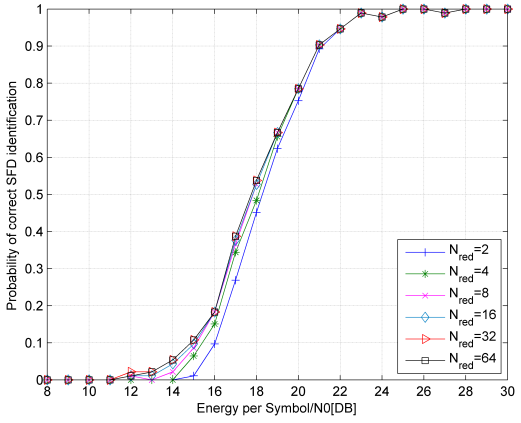


(c) $T_{int1}$=8ns.

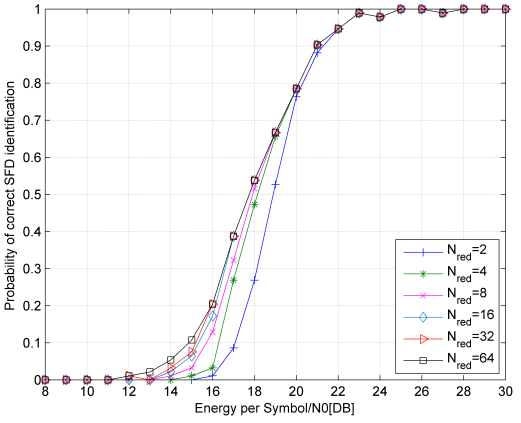


(d) $T_{int1}$=16ns.

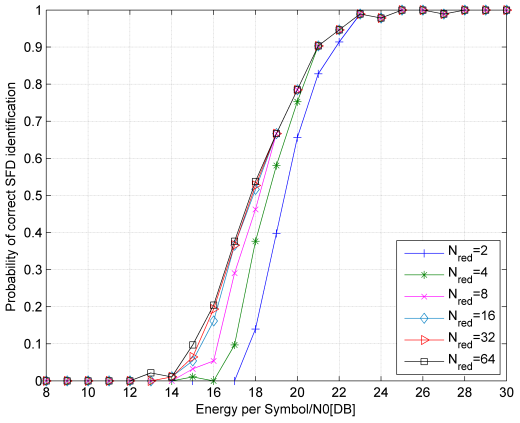


(e) $T_{int1}$=32s.

Figure 4.4: Correctly identifying the short SFD with positive acquisition at different $T_{int1}$.

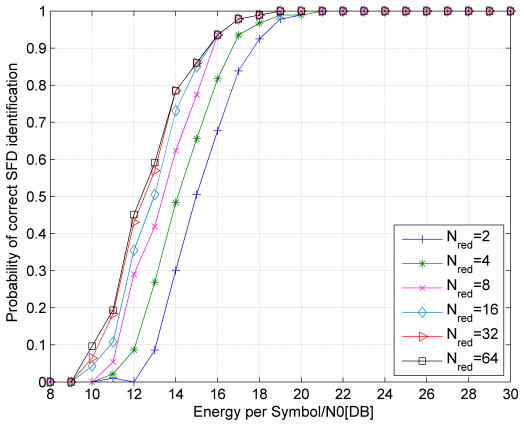


(a) $T_{int1}$=2ns.

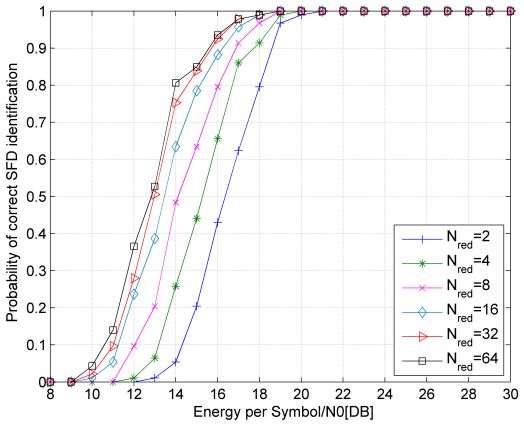


(b) $T_{int1}$=4ns.

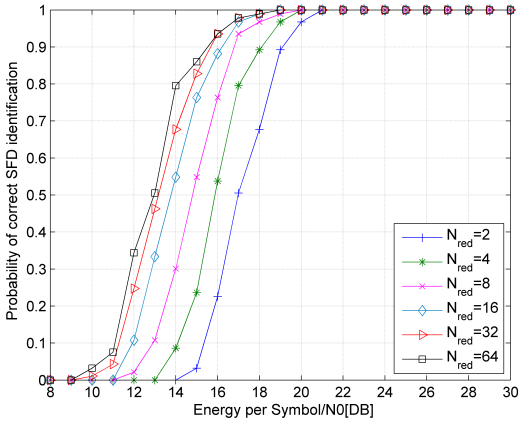


(c) $T_{int1}$=8ns.

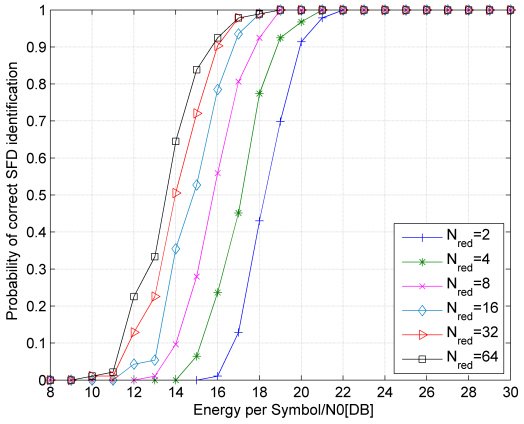


(d) $T_{int1}$=16ns.

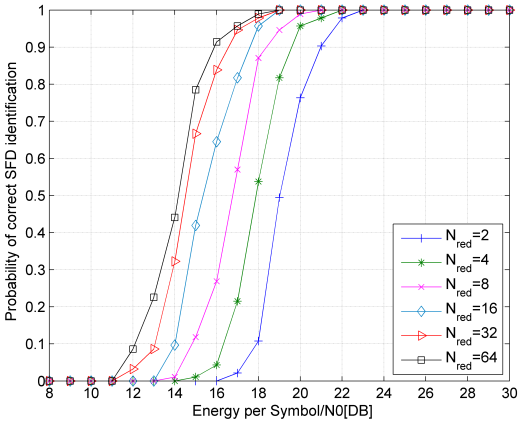


(e) $T_{int1}$=32s.

Figure 4.5: Correctly identifying the long SFD with positive acquisition at different $T_{int1}$.

finding that very peak in the relevant search area also decreases and in equal measure the probability of choosing the wrong peak increases. Even though the length of the search area declines when using the short SFD and therefore less samples have to be taken into consideration for the maximum search, the processing gain achieved by combining more symbols outweighs the smaller chance of wrong identification due to fewer choices for the short SFD-case.

What can be seen is that the short SFD can only be found at high SNR and therefore setting $N_{sfd}$ to eight might not be a good choice for ranging purposes. In Figure 4.4 (a) it can be seen that the search for the start of the SFD really is the limiting factor and so the outcome is the same for all $N_{red}$ at $T_{int1}$=2 ns. For higher $T_{int1}$ a performance difference can be observed with respect to $N_{red}$, due to the fact that the detection performance suffers with longer integration times and therefore the limiting factor for the overall outcome shifts from SFD search to the number of symbols used to trigger the detection process the longer the integration period becomes. The same holds for the long SFD where in Figure 4.5(a) the outcome for $N_{red}$=64 and $N_{red}$=32 fall together which are again drawn apart at higher integration periods. This indicates that using more symbol repetition in the SYNC portion for acquisition purposes is rendered useless when ranging is performed with the SFD symbols.

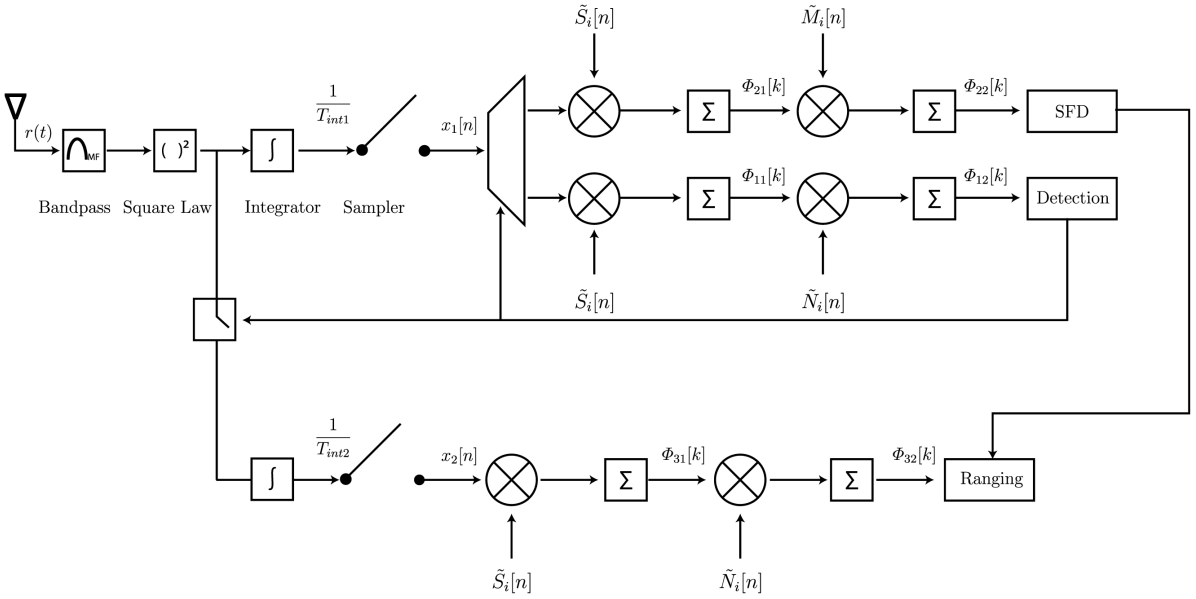


Figure 4.6: Ranging Algorithm II

## 4.3 Ranging Algorithm II

The main idea of RA II is to benefit from information from the detection process and to take advantage of the perfect autocorrelation feature of the TPS in order to reduce the total number of operations needed to perform ranging. While RA I switches to shorter integration time and therefore higher time resolution immediately after a detection event, the second proposed algorithm takes a slightly different approach. After successful detection of a signal, which is done at a long integration time $T_{int1}$, the process is split into two paths. The search for the SFD is also carried out at $T_{int1}$ as, resulting in an area of uncertainty of twice the integration time for the position of the SFD. This alone would result in a high mean average error for ranging, so a second operation has to be carried out to further determine the exact TOA. This is done by the second signal flow path which is also initialized by the detection part. At the same time the search for the SFD starts, the second process begins integrating with $T_{int2} = T_p$, ensuring high temporal resolution for ranging purposes. This process again correlates the signal with the TPS, but uses the SYNC template for the second correlation, assuming that at the point in time detection took place, a certain number of the SYNC symbols have not yet been processed, leaving those remaining symbols for further processing. Those two

operations together would cause more processing steps than the processing in RA I, if no further steps would be taken to reduce complexity by exploiting the perfect correlation features of the TPS. The sample where detection takes place is at the same time the position of one of the preamble symbols. This symbol is denoted as the $q$th SYNC symbol. With the knowledge of the approximate position of that symbol, the detector can rule out and subsequently exclude the samples that lie between two consecutive preamble symbols, when it comes to energy combination across symbols by the second correlator. So because of the perfect autocorrelation feature of the ternary code and the knowledge of the symbol's position within an area of uncertainty of length $2T_{int1}$, the second correlator can restrict its operation on the area where symbol energy is assumed. By excluding most of the noise samples, the total number of operations can be reduced substantially. A detailed complexity analysis will follow in the next section. The state diagram of the ranging process in RA II is shown in Figure 4.7.

A delay is implemented to avoid getting a peak from the tail of the $q$th symbol but rather determine the position of the next symbol $(q+1)$. The maximum of the second SYNC correlator's output, when triggered by the detection process and restricted to a certain area, can be assumed to be the position of the $(q+1)$th SYNC symbol, with a reduced uncertainty due to shorter $T_{int2}$. Having estimated the SYNC symbol position by a maximum search and the estimated TOA by a search back window, the final step is to combine the TOA of this very symbol with its distance to the start of the SFD.

This has to be done, because the start of the SFD is the unique reference point in this work for both ranging and future positioning purposes and at this point its position is only known with uncertainty of $2T_{int1}$.

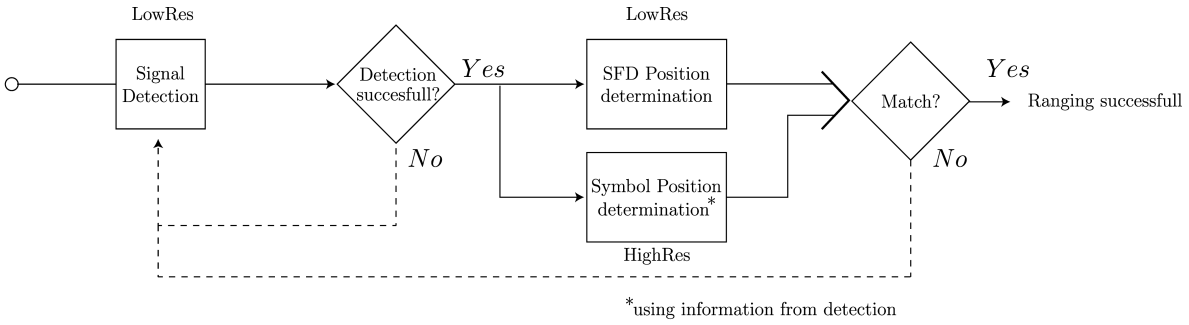


Figure 4.7: State diagram for RAII

The mathematical description of the output of the SFD correlator is given in the

following equation, which is the same as (4.1), with the only difference being the low time resolution resulting in fewer discrete samples that have to be processed:

$$\Phi_{22}[k] = \sum_{n=0}^{k+(N_{sfd}N_c)-1} \Phi_{21}[n+k]\tilde{M}_i[n] \tag{4.9}$$

The approximate start of the SFD at sample $k_{sfd}$ is found by a maximum search

$$k_{sfd} = \arg\max_k \Phi_{22}[k]\Big|_{k_{det1}+\frac{N_{sync}T_{psym}}{T_{int1}} \leq k \leq k_{det1}+\frac{(N_{sync}+N_{sfd})T_{psym}}{T_{int1}}} \tag{4.10}$$

The second path correlates with the bipolar sequence

$$\Phi_{31}[k] = \sum_{n=0}^{k+(N_c-1)} x_2[n+k]\tilde{S}_i[n] \tag{4.11}$$

and then performs the second correlation with a SYNC template of reduced symbol repetitions $N_{red}$

$$\Phi_{32}[k] = \sum_{n=0}^{k+(N_{red}N_c)-1} \Phi_{31}[n+k]\tilde{N}_i[n] \tag{4.12}$$

with $N_{red} = N_{sync} - q$ because of the assumption that the detection process has successful ended after the $q$th symbol. With the knowledge of the position of sample $k_{det1}$ - denoting the sample where the detection process is triggered - the ranging algorithm has to perform processing $\Phi_{32}[k]$ only for samples k with

$$k_{det2} - \frac{T_{int1}}{T_{int2}} \leq k \leq k_{det2} + \frac{T_{int1}}{T_{int2}} \tag{4.13}$$

where $k_{det2}$ is the high resolution counterpart of $k_{det1}$. Again a maximum search is carried out to determine the sample that corresponds to the position of the $(q+1)$th SYNC symbol. Having obtained the peak resembling the position of the $(q+1)$th symbol, the already known search back window is used to determine the leading edge of the signal and with that an estimation for the TOA $k_{toa}$ of that very symbol.

$$k_{q+1} = \arg\max_k \Phi_{32}[k] \tag{4.14}$$

$$k_{toa} = \arg\min_k \{k|\Phi_{32}[k] > \gamma_{LE}\}\Big|_{(k_{q+1}-w_{sb}) \leq k \leq k_{q+1}} \tag{4.15}$$

Figures 4.8 and 4.9 give an overview over the area of the signal between symbols that is not processed by RA II. In Figure 4.8 the symbol's position in $\Phi_{22}[k]$ is illustrated with

the corresponding samples from the detection process, while in Figure 4.9 the samples of $\Phi_{31}[k]$, which do not need to be processed, are shown. The area of length $T_{psym} - 2T_{int1}$ that lies between two consecutive preamble symbols is excluded from energy combination. The only thing left to do, is to match the position of the $(q+1)$th symbol with the position of the SFD. This is done by comparing that distance with multiples of the known symbol duration $T_{psym}$. From comparing, one can determine the position of the SFD with the same amount of accuracy as the position of the $(q+1)$th symbol.

The distance $d_{sfd}$ in samples between the TOA of the $(q+1)$th symbol and the start of the SFD is calculated by

$$d_{sfd} = k_{sfd}\frac{T_{psym}}{T_{int2}} - k_{toa} \tag{4.16}$$

The TOA of the SFD can then be found by

$$k_{toasfd} = k_{toa} + \left\lceil \frac{d_{sfd}}{\frac{T_{psym}}{T_{int2}}} \right\rceil \frac{T_{psym}}{T_{int2}} \tag{4.17}$$

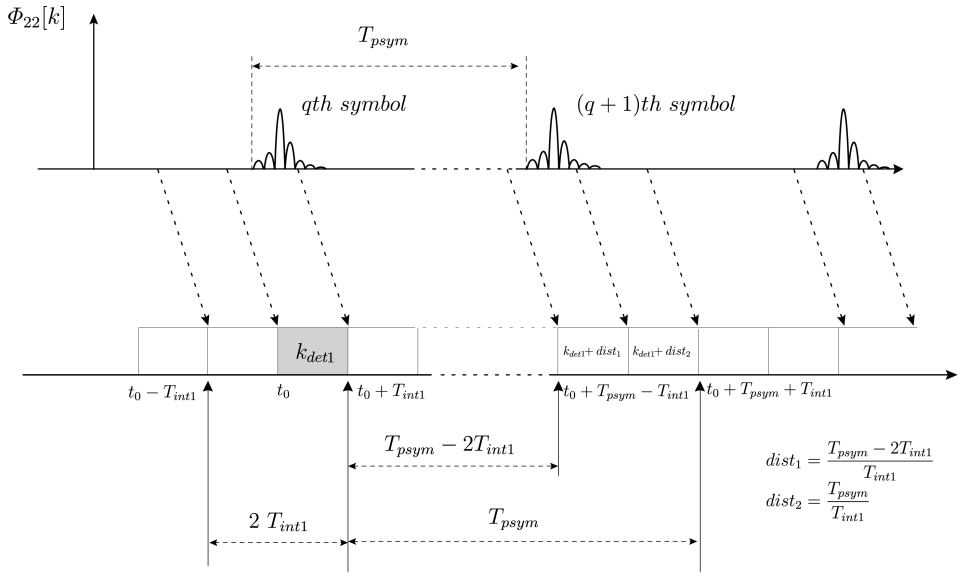


Figure 4.8: Symbol Position and corresponding integration intervals.

The SFD position is then used to calculate the distance between transmitter and receiver by multiplying the time of flight by the speed of light. While for ranging only one set of ranging data is necessary to calculate the distance, for two-dimensional positioning one needs to have at least three sets of data that need to be combined in order to specify the sender's or receiver's position.

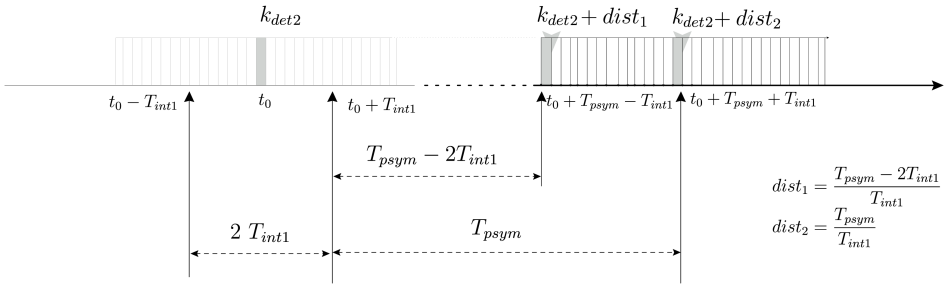


Figure 4.9: Samples not evaluated by RA II.

### 4.3.1 Simulation Results

Numerical simulations have been done by using MATLAB to compare the ranging properties of the two algorithms. While in previous simulations the results were given in percentage of successful detection, this time they are illustrated as mean average error (MAE) as well as number of outcomes with an ranging error smaller than one meter. With the results from the previous simulations, the possible combinations of system parameters have been limited to number of SYNC symbols $N_{sync} = 64$ for the long and $N_{sync} = 8$ the short SFD symbol number $N_{sfd}$. This time, the detection process is assumed to have positively triggered detection after $\frac{N_{sync}}{2}$ for both RAs at an integration period $T_{int} = 32ns$, leaving $q = \frac{N_{sync}}{2}$ symbols for ranging purposes. A searchback window of length 32ns is used with the parameter $c = 0.5$. The simulations have been made with 105 impulse responses from a line-of-sight (LOS) and a non-line-of-sight (NLOS) scenario each [GBG+09]. The corresponding results are shown separately.

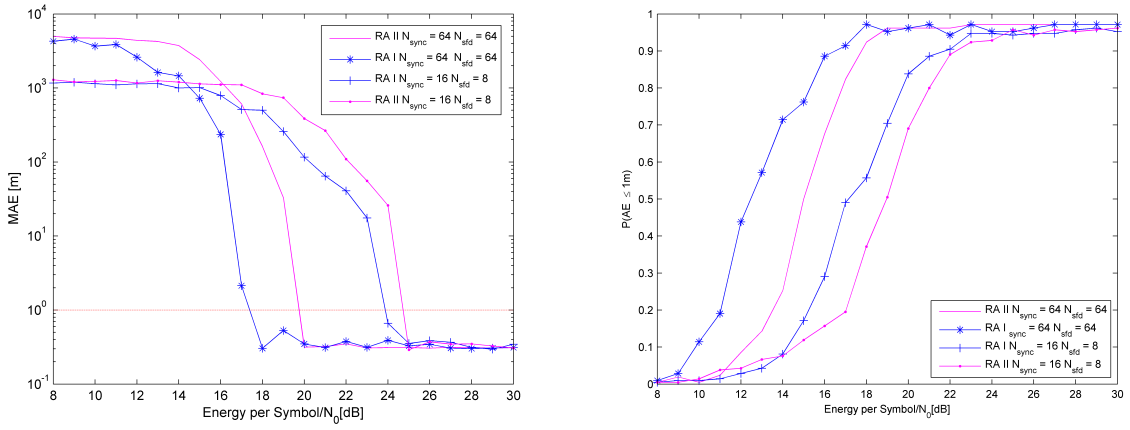


(a) Mean Average Ranging Error.

(b) Error smaller than one meter.

Figure 4.10: LOS

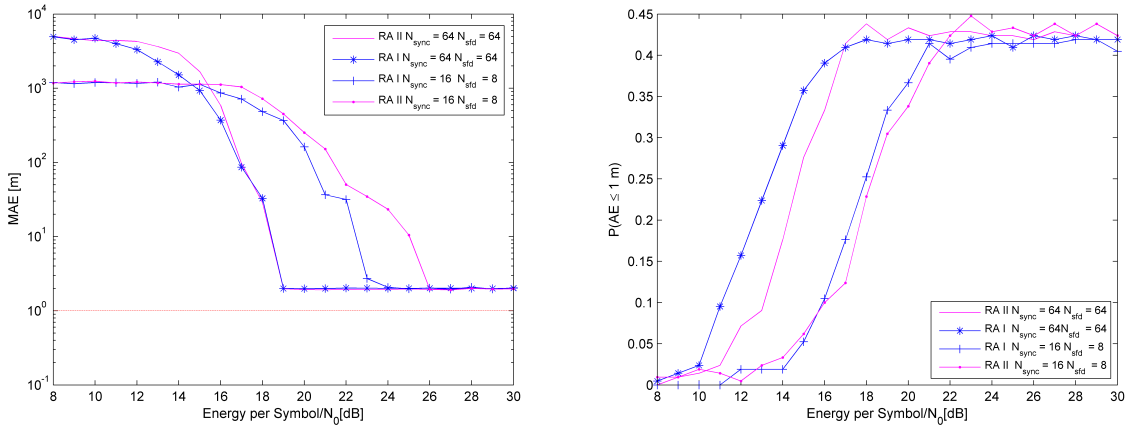


(a) Mean Average Ranging Error.

(b) Error smaller than one meter.

Figure 4.11: NLOS

What can be observed by the results, is that RA I performs slightly better than the second one in terms of robustness, meaning that the achieved mean average error (MAE) for low SNR is smaller than the error caused by RA I. This can be explained by the fact that RA II hast to find the SFD's start position at long integration time $T_{int1}$, increasing the chance that for the maximum search that the highest peak does not resemble the SFD, resulting in a wrong assumption of the SFD's position and consequently in a wrong matching of the distance between the SFD and SYNC symbol. The trade-off between fewer mathematical operations and ranging capabilities results in different curves for the two RAs. The comparison in complexity for the two RAs is made in the next subsection.

The reason for the smaller MAE at low SNR when using the shorter SFD can be explained by the smaller area where the maximum search is carried out, thus resulting in a lower error when a global ranging error occurs. For high SNR both algorithms achieve the same accuracy, because the fundamental concept for both RAs is basically the same. When it comes to NLOS environments, the SNR requirement for robust ranging is significantly higher than that for LOS environments. Another limiting factor for NLOS is the deficiency of the searchback window which results in fewer outcomes with an error smaller than one meter as it is intended by the standard (see Figure 4.11). That is due to the fact that when the backwards search is carried out for an NLOS scenario it happens more often that the sample at the time-of-arrival contains too little energy and therefore lies below the threshold $\gamma_{LE}$ then in LOS scenarios.

## 4.4 Complexity Analysis

The RAs' complexities are investigated in this Section on a high-level abstraction by comparing the total number of operations (NoO) needed to achieve ranging as a function of the used system parameters of the 802.15.4a standard, as well as different integrations times $T_{int1}$. The analysis is limited on the ranging process itself under the assumption that the effort for the detection process in terms of operations is the same for both RAs.

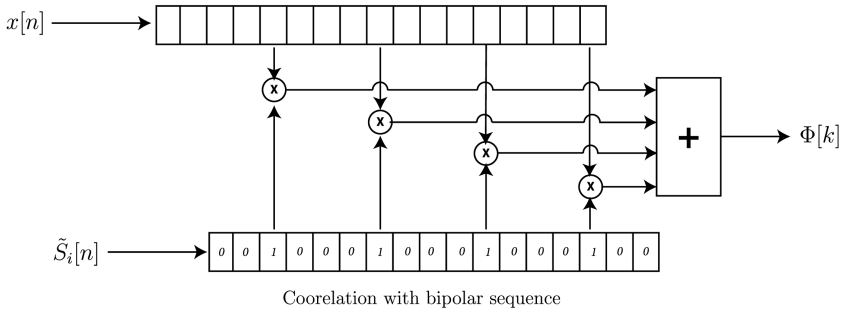


Figure 4.12: Fundamental structure of a correlator [Gei09a].

Figure 4.12 illustrates the main calculation steps needed for correlation. The already integrated and sampled signal $x[n]$ gets multiplied by the known symbol sequence. For every outcoming sample of $\Phi[k]$, $x[n]$ has to be multiplied by the bipolar sequence $\tilde{\mathbf{S}}_i$, resulting in $N_{code}$ single multiplications that have to be added up in the same amount of additions to produce a single result in $\Phi[k]$. The zero samples in $\tilde{\mathbf{S}}_i$ caused by the additional $(L-1)$ zeros inserted in between by the spreading process are not taken into considerations for the total NoO because of the assumption that the result of a zero multiplication is known in advance.

That leads to the total NoO for one result in $\Phi[k]$ with

$$\overbrace{N_{code}^{\alpha}}^{Multiplications} + \overbrace{N_{code}}^{Additions} = 2N_{code} \tag{4.18}$$

where $\alpha$ denotes a weight factor accounting multiplication, because multiplications are quadratic in complexity [Aic06]. In this case, $\alpha$ is set to one because there are only operations where the multiplier is $\in \{1, -1\}$, thus leading to a simple inversion process for the second case resulting in a simplification for the total NoO needed for one outcome sample.

This has to be repeated for the length of the signal, and for RA I this leads to $N_{RA21}$ numbers of operations for the computation of $\mathbf{\Phi}_{21}$ described in (4.19). The nomenclature

complexity calculations $N_{RA}$ is adopted from the naming of the correlation processes for the RAs like depicted in the Figures 4.1 and 4.6.

$$N_{RA121} = 2N_{code} \overbrace{\left(\frac{N_{sync}}{2} + N_{sfd}\right) LN_{code} \frac{T_p}{T_{int2}}}^{Length} \tag{4.19}$$

The ratio pulse duration to integration time $T_p/T_{int2}$ reduces the total NoO when ranging is performed at longer integration times than the pulse duration.

The second correlation has to be performed using the SFD template resulting in

$$\overbrace{N_{sfd}^{\alpha}}^{Multiplications} + \overbrace{N_{sfd}}^{Additions} = 2N_{sfd} \tag{4.20}$$

operations for a single outcome. Again setting $\alpha = 1$ simplifies the equation leading to

$$N_{RA122} = 2N_{sfd} \left(\frac{N_{sync}}{2} + N_{sfd} - 1\right) LN_{code} \frac{T_p}{T_{int2}} \tag{4.21}$$

The total NoO is

$$N_{RA1} = N_{RA121} + N_{RA122} \tag{4.22}$$

The second RA performs the same operations as described in Equation (4.19), with the difference being fewer samples that need to be processed due to the longer integration period $T_{int1}$. So the number of samples where this operation is carried out is reduced by a factor that is the ratio of the pulse duration to the the longer integration period.

$$N_{RA221} = 2N_{code} \left(\frac{N_{sync}}{2} + N_{sfd}\right) LN_{code} \overbrace{\frac{T_p}{T_{int1}}}^{Reduction factor} \tag{4.23}$$

The same factor shortens the second correlation, leading to

$$N_{RA222} = 2N_{sfd} \left(\frac{N_{sync}}{2} + N_{sfd} - 1\right) LN_{code} \frac{T_p}{T_{int1}} \tag{4.24}$$

For the second signal path, where the position of one SYNC symbol is determined relative to the position of the start of the SFD, the bipolar correlation has to be carried out over the remaining SYNC symbols.

$$N_{RA231} = 2N_{code} \frac{N_{sync}}{2} LN_{code} \frac{T_p}{T_{int2}} \tag{4.25}$$

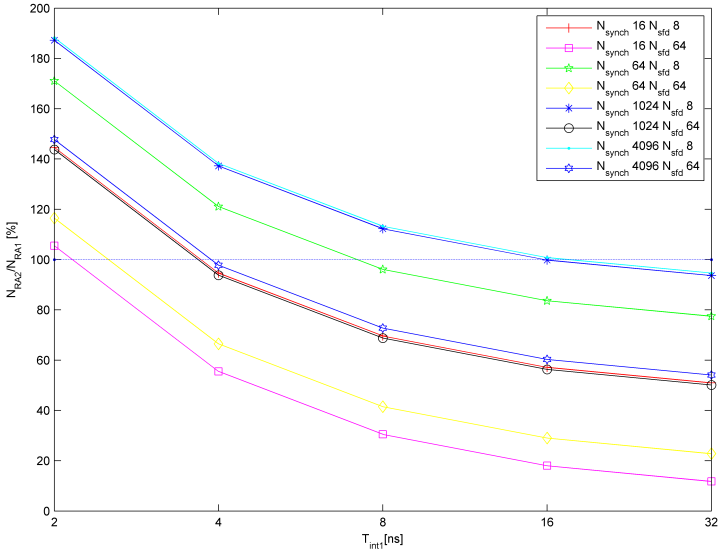


(a) Ratio of NoO RAII to RAI

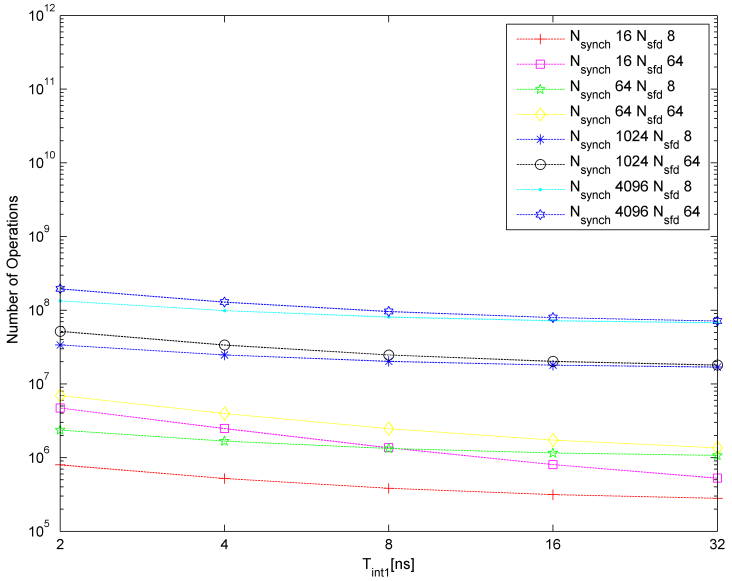


(b) Total NoO needed for RAII

Figure 4.13: Results complexity analysis

Energy combination across symbols now is restricted to the area of uncertainty $2T_{int1}$ concerning the position of a single SYNC symbol.

$$N_{RA232} = (N_{code} + 1)\, L N_{code} \overbrace{\frac{2T_{int1}}{T_{psym}}}^{reduction factor} \frac{T_p}{T_{int2}} \tag{4.26}$$

The overall number of operations is the sum over the single steps and given by

$$N_{RA2} = N_{RA221} + N_{RA222} + N_{RA231} + N_{RA232} \tag{4.27}$$

Figure 4.13 (a) shows the ratio $\frac{N_{RA2}}{N_{RA1}}$ for all possible combinations of system parameters $N_{sfd}$ and $N_{sync}$ plotted against increasing integration time $T_{int1}$. It can be seen that for different system parameters the integration time needed for undercutting RA I varies. For the parameters used in the previous section to perform simulations, the complexity of RA II is reduced to approximately 20% of that from RA I. It can be seen that the second algorithm is able to reduce complexity the most when the length of the SYNC portion is in a reasonable proportion to that of the SFD. This is because the most retrenchments are achieved on the SFD part due to the longer integration time. When the SYNC portion becomes longer, the total number of operations rises and the reduced processing on the SFD does not outweigh the increased processing on the SYNC part anymore.

Figure 4.13 (b) shows the total NoO needed to achieve ranging with the second algorithm as a function of the integration time $T_{int1}$ used in the SFD path of RA II. The intersecting curves for the parameter combinations $(N_{sync} = 16, N_{sfd} = 64)$ and $(N_{sync} = 64, N_{sfd} = 8)$ at approximately $T_{int} = 8$ns are due to the assumption taken for the detection process to have successfully ended after $\frac{N_{sync}}{2}$ symbols.

# Chapter 5

# Positioning

## 5.1 Overview

In this Chapter the previously introduced ranging algorithms are used to achieve two-dimensional positioning for a real life system. In this system the transmitter serves as a mobile whose location can be observed by the means of a tracking system. The tracking system consists, besides the transmitter (mobile), of three receivers at fixed (known) locations - from now on referred to as base stations (BS). For two-dimensional positioning, at least three BSs are needed to calculate the position of the mobile device. The systems relies on a time-based approach, known as the time difference-of-arrival (TDOA) technique, which uses the observed-time-difference (OTD) from two BSs. The OTD is caused by a difference in distance between the mobile and the particular BS. This information defines a hyperbolic function [GG03] and with an additional OTD information, a second hyperbola is obtained that intersects with the first in a point that determines the position of the mobile.

Additionally to that, a graphical user interface is implemented in MATLAB that serves as a real time feedback monitor, illustrating the mobile's position.

## 5.2 Time-Difference-of-Arrival

The TDOA technique is along with the time-of-arrival (TOA) technique, one of the time based approaches to positioning. Both have in common that they use the signal's travel time [GTG+05] for location estimation. Unlike TOA which relies on a common clock among the mobile and the BSs to determine the mobile's position, TDOA can still be

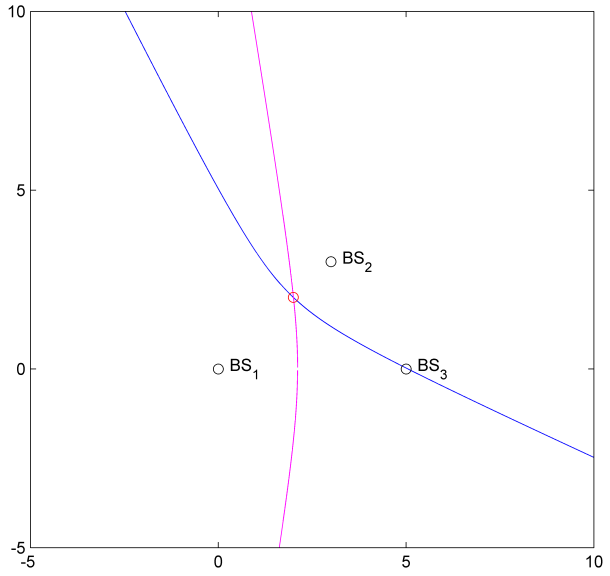


Figure 5.1: Hyperbolic functions representing constant TDOA

used in the absence of synchronization, as long as there is a shared clock among the BSs. The OTD between two BSs results in an area of possible locations for the mobile. This area has the property that for every point in it, the difference in distance to the two BSs is constant and therefore is given by a hyperbola with the BSs at its foci. By using three BSs, two hyperbolas can be obtained giving the position of the mobile at their intersection. This is illustrated in Figure 5.1. Since the delay measurements are not free of error and since the resulting hyperbolas might intersect at more than one point, an iterative algorithm is used to find the correct intersection point. The mathematical description can be found in the following subsection.

### 5.2.1 TDOA Iterative Algorithm

The TDOA $T_{ij}$ of a signal impinging at the Base stations $BS_i$ and $BS_j$ can be calculated by

$$T_{ij} = \tau_i - \tau_j = \frac{D_{ij}}{c} \tag{5.1}$$

where $c$ is the electromagnetic propagation speed ($c \approx 3 \times 10^8$ ms$^{-1}$), $\tau$ is the absolute propagation delay and $D_{ij}$ is the absolute difference in meter [SM98].

Equation (5.2) shows the relative distance on BS$_i$ and BS$_j$, which defines a hyperbola in the |XY|-plane with foci at the two BSs, where $x, y$ are the yet unknown coordinates

of the mobile and $x_i, y_i$ and $x_j, y_j$ are the positions of $BS_i$ and $BS_j$, respectively.

$$D_{ij} = \sqrt{(x - x_i)^2 + (y - y_i)^2} - \sqrt{(x - x_j)^2 + (y - y_j)^2} \tag{5.2}$$

Since more than two BSs are available, a set of non-linear equations is formalized in (5.3) and (5.4).

$$D_{ab} = \sqrt{(x - x_a)^2 + (y - y_a)^2} - \sqrt{(x - x_b)^2 + (y - y_b)^2} \tag{5.3}$$

$$D_{ac} = \sqrt{(x - x_a)^2 + (y - y_a)^2} - \sqrt{(x - x_c)^2 + (y - y_c)^2} \tag{5.4}$$

As linearization point $x_0, y_0$, the mean position of the BSs is selected and the linear representation can be written according to [Gig06] as

$$D = f(x, y) = f(x_0, y_0) + \left.\frac{\partial f}{\partial x}\right|_{x_0,y_0} (x - x_0) + \left.\frac{\partial f}{\partial y}\right|_{x_0,y_0} (y - y_0) \tag{5.5}$$

where $f(x_0, y_0)$ is the result of (5.2) by inserting the linearization point in the non-linear equation and $\left.\frac{\partial f}{\partial x}\right|_{x_0,y_0}$ is the derivative of $f$ in x-direction. The derivatives are represented by Equations (5.6) and (5.7).

$$\left.\frac{\partial f}{\partial x}\right|_{x_0,y_0} = \frac{x - x_i}{\sqrt{(x - x_i)^2 + (y - y_i)^2}} - \frac{x - x_j}{\sqrt{(x - x_j)^2 + (y - y_j)^2}} \tag{5.6}$$

$$\left.\frac{\partial f}{\partial y}\right|_{x_0,y_0} = \frac{y - y_i}{\sqrt{(x - x_i)^2 + (y - y_i)^2}} - \frac{y - y_j}{\sqrt{(x - x_j)^2 + (y - y_j)^2}} \tag{5.7}$$

Equation (5.5) can be rewritten to (5.8) and further, because $f(x_0, y_0)$, $\left.\frac{\partial f}{\partial x}\right|_{x_0,y_0} x_0$ and $\left.\frac{\partial f}{\partial y}\right|_{x_0,y_0} y_0$ are known, to (5.9) [Gig06].

$$D = f(x_o, y_0) + \left.\frac{\partial f}{\partial x}\right|_{x_0,y_0} x - \left.\frac{\partial f}{\partial x}\right|_{x_0,y_0} x_0 + \left.\frac{\partial f}{\partial y}\right|_{x_0,y_0} y - \left.\frac{\partial f}{\partial x}\right|_{x_0,y_0} y_0 \tag{5.8}$$

$$D' = D - f(x_0, y_0) + \left.\frac{\partial f}{\partial x}\right|_{x_0,y_0} x_0 + \left.\frac{\partial f}{\partial y}\right|_{x_0,y_0} y_0 \tag{5.9}$$

with

$$D' = \left.\frac{\partial f}{\partial x}\right|_{x_0,y_0} x + \left.\frac{\partial f}{\partial y}\right|_{x_0,y_0} y \tag{5.10}$$

By obtaining the equations for both BS pairs, a linear equation system can be built.

$$D' = \mathbf{A}\underline{\tilde{x}} = \begin{pmatrix} \frac{\partial f_1}{\partial x}\Big|_{x_0,y_0} & \frac{\partial f_1}{\partial y}\Big|_{x_0,y_0} \\ \frac{\partial f_2}{\partial x}\Big|_{x_0,y_0} & \frac{\partial f_2}{\partial y}\Big|_{x_0,y_0} \end{pmatrix} \underline{\tilde{x}} \tag{5.11}$$

The system solved with respect to $\underline{\tilde{x}}$ results in

$$\underline{\tilde{x}} = (\mathbf{A}^\mathbf{T}\mathbf{A})^{-1}\mathbf{A}^\mathbf{T}D' \tag{5.12}$$

where $\underline{\tilde{x}}$ contains the estimated coordinates for the mobile $\underline{\tilde{x}} = [\tilde{x}, \tilde{y}]^T$. This result serves as starting point for the next iteration of the algorithm. The iteration proceeds until convergence is achieved.

## 5.3 Experimental Setup

For practical evaluation, a tracking system is set up in the HF-laboratory at the SPSC. Signal generation according to the IEEE 802.15.4a standard is performed by the demonstrator system [Buc08]. The output is upconverted and then sent via the transmitter antenna according to FCC/EC regulations (see B.3). As reference BSs, three antennas are set up within the laboratory at known positions. The received signals from the three BSs are then fed into a digital sampling oscilloscope (DSO), where the signal is digitized and temporarily stored. The post processing is done on a personal computer (PC) which also triggers the DSO's acquisition process by means of user input, and then acquires the data from the scope via a local area network connection by TCP/IP for further processing. A more detailed description of the setup can be found in the appendix together with delay profiles of the used cables as well as the used amplifier and filter.

The IEEE 802.15.4a frame is generated continuously with a short intermission between two consecutively sent frames. Since there is no cable-based synchronization between sender and receiver (DSO), the signal acquisition starts at a random point. To ensure that at least one entire frame is captured by the DSO, the capture span is set to the length of two frames plus the length of the intermission that lies in between. This ensures that one frame is captured as a whole.

Prior to the positioning, preprocessing is carried out over the whole captured signal to determine the start position of the uncut frame. This has to be done because the setup was intended to work without a trigger signal from the sender. If it was not for the absence of that trigger, preprocessing could be skipped, because the captured signal would always start at the beginning of the frame and capture duration could be adjusted

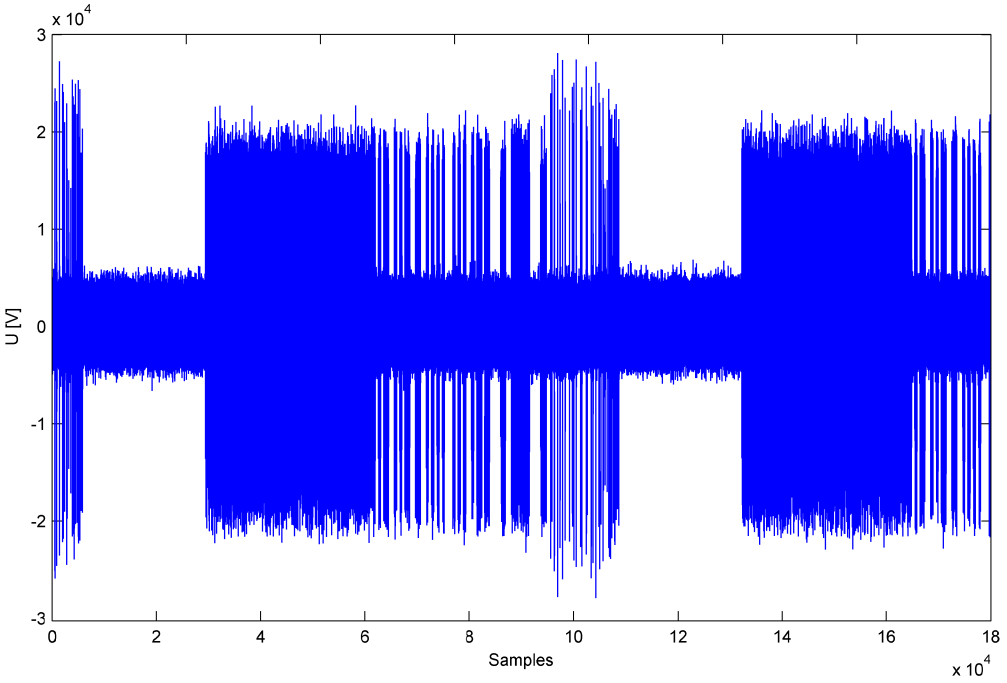


Figure 5.2: Captured signal.

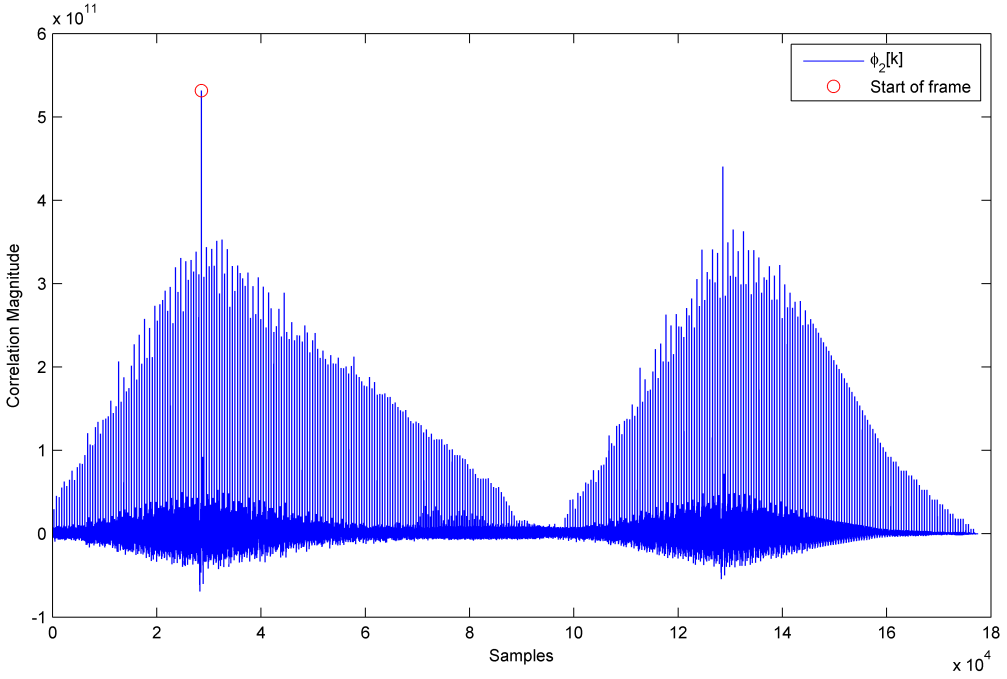


Figure 5.3: Output of preprocessing with indicated start position of the frame.

to the length of a single frame. In order to determine the start of the uninterrupted frame, a two step correlation, first on chip and second on symbol level, is performed, using both the SYNC and the SFD symbols for energy combination. The maximum of the second correlation is considered to be the start of the uninterrupted frame. An exemplary output of the preprocessing step is depicted in Figure 5.3. With the knowledge of the frame's start position and its length the desired signal is cropped and further passed on to the detection part, where the frame's presence is sensed by using the acquisition threshold from Chapter 3.

Positioning is done by processing the signal with either RA I or RA II, combining the resulting ranging markers in each case and performing the TDOA algorithm. The result is then, together with the BS positions, illustrated in a MATLAB-based GUI.

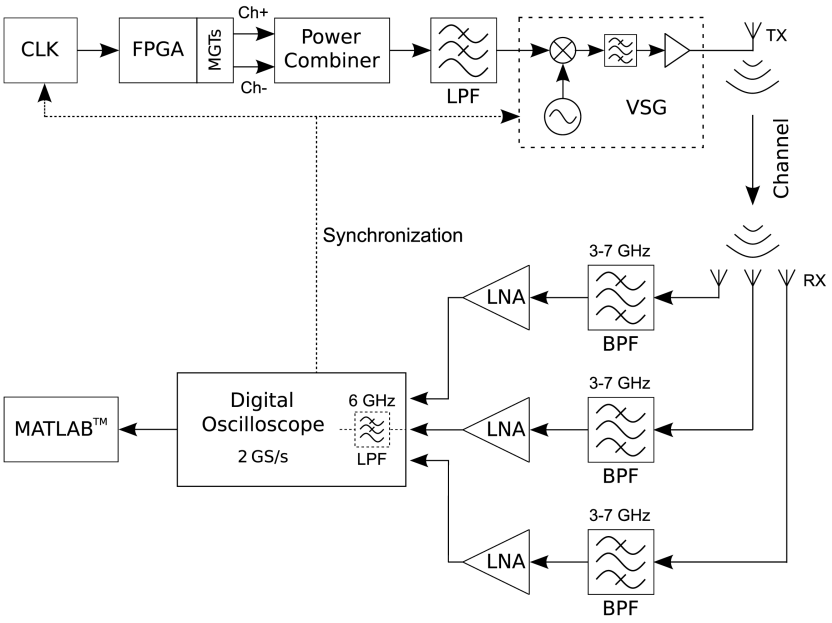


Figure 5.4: Overview of the measurement setup [GBG+09].

## 5.4 Measurements

Two scenarios are investigated during the measurement, one LOS and one NLOS case. In the latter, one BS was blocked by a human head. For each scenario 168 single measurement points are taken by placing the mobile along a 21×8 grid. The grid shows a 0.1m spacing and each point's location is perfectly known within the local coordinate system. In Figure 5.5 the floor plan is illustrated. The three BSs span a triangle with the grid approximately in its center. A more detailed description can be found in Appendix B.

The demonstrator is set to generate an IEEE 802.15.4a compliant signal with $N_{sfd} = 64$ and $N_{sync} = 64$ resulting in 128 symbols for frame start detection. The spacing $L$ is set to 16, the used code is the length 31-ternary sequence $C_6$. The signal is upconverted to 4.5GHz then sent via the transmitter antenna, received at the BSs and (under)sampled with the DSO sampling rate set to 2 GS/s, temporarily stored and then transferred to the PC where positioning is performed. The false alarm probability for detection is set to $P_{FA} = 10^{-8}$, $N_{red} = 32$, the search back window length to 32ns and $c = 0.5$ for calculating $\gamma_{LE}$.

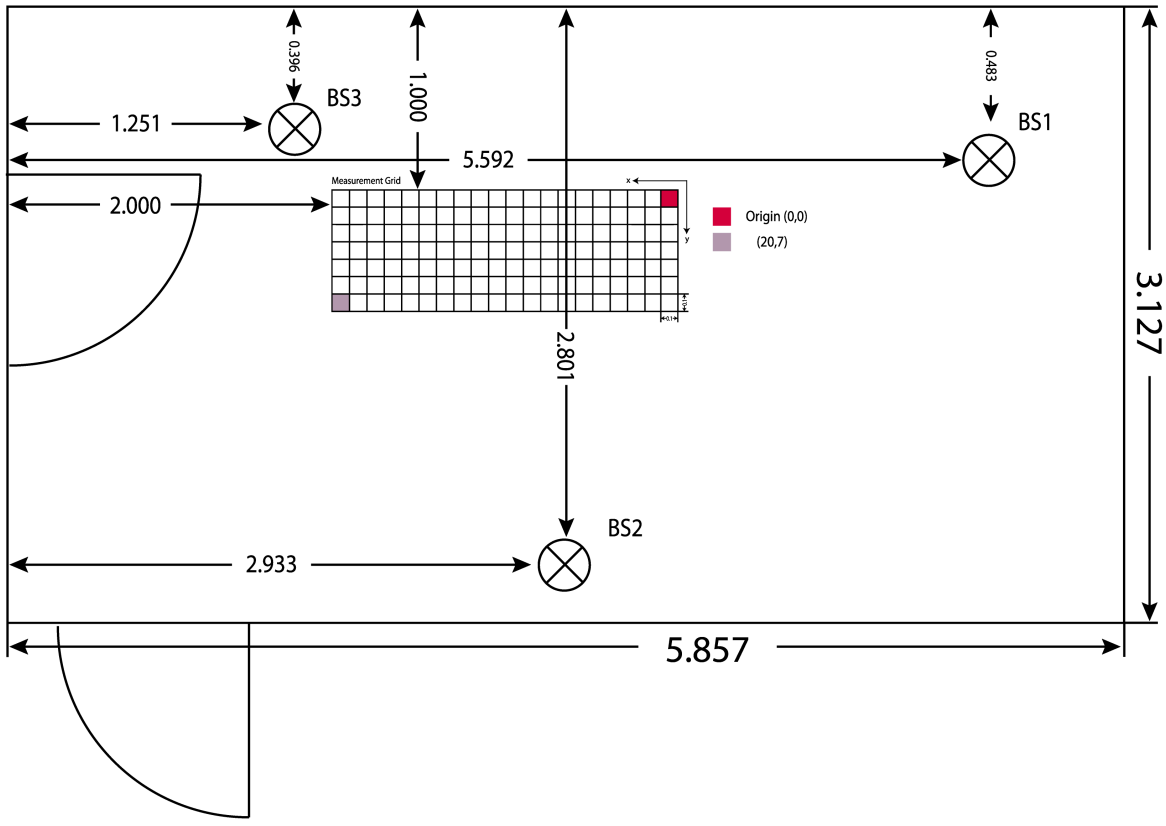


Figure 5.5: Floor plan showing the the measurement grid and the BSs (all distances in meter).

## 5.5 Results

Positioning based on the two presented has been done for both the LOS and the NLOS scenario. The resulting positioning error depicted as cumulative distribution functions

(CDF) in Figure 5.6 confirms that the two RAs' performance in terms of accuracy is basically the same, just like the previously conducted simulations have led to believe. Positioning is performed for ranging $T_{int2} = \{1, 2, 4\}$ns. Both RAs' performance is better for the LOS case, because in the NLOS scenario the SB-algorithm sometimes fails to correctly identify the leading edge and therefore causes a larger error. The CDFs show that for both cases and for both RAs approximately 90% of the positioning results show an error of less than half a meter for $T_{int2} = \{1, 2\}$ns, and with that satisfy the aim of the IEEE 802.15.4a standard for positioning with sub-meter accuracy.

Figures 5.7 and 5.8 illustrate color-coded the positioning error within the used measurement grid. Since the grid is located in the middle of the triangle that is spanned by the three BSs no significant influence of the geometric setup is observed. The main source of error shows to be the quantization of the OTD, which of course leads to increasing errors with longer quantization time. The NLOS-scenario results show a larger positioning error than the LOS scenario. As mentioned, this is caused by the deficiency of reliably detecting the leading edge by the searchback window algorithm.

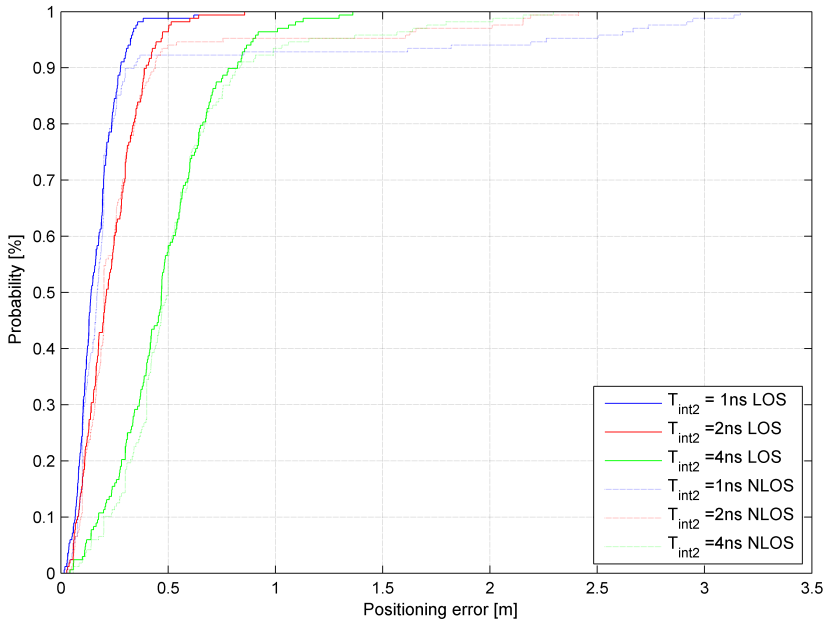


(a) RA I

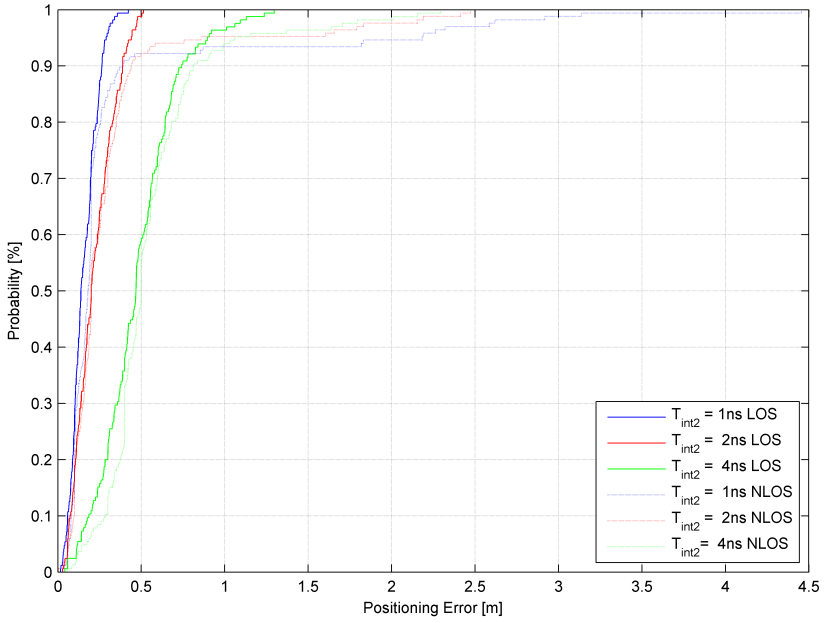


(b) RA II

Figure 5.6: CDFs showing Positioning Error.

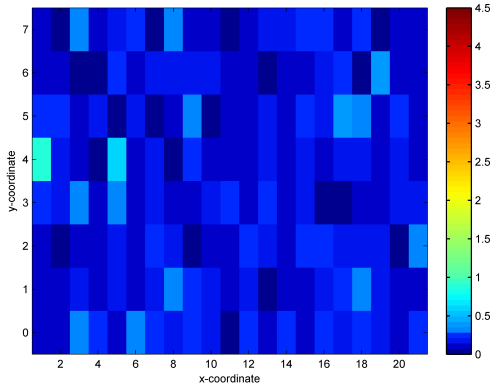


(a) RA I $T_{int2} = 1$ns.

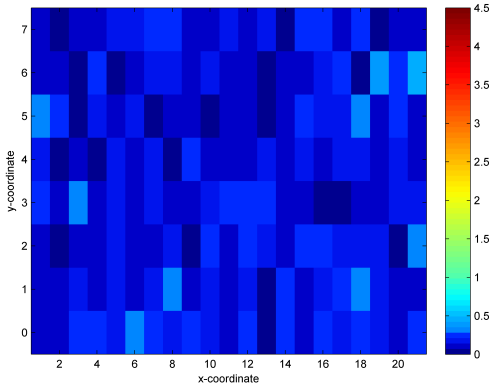


(b) RA II $T_{int2} = 1$ns.

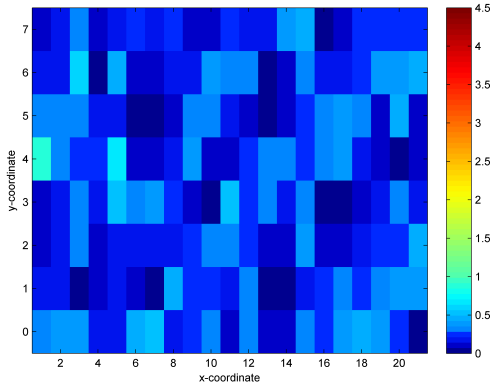


(c) RA I $T_{int2} = 2$ns.

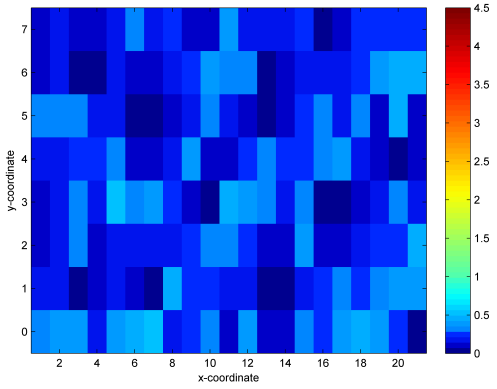


(d) RA II $T_{int2} = 2$ns.

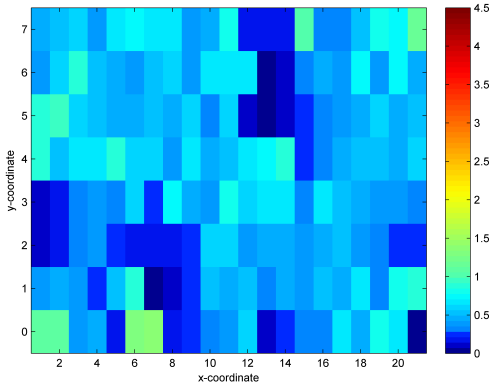


(e) RA I $T_{int2} = 4$ns.

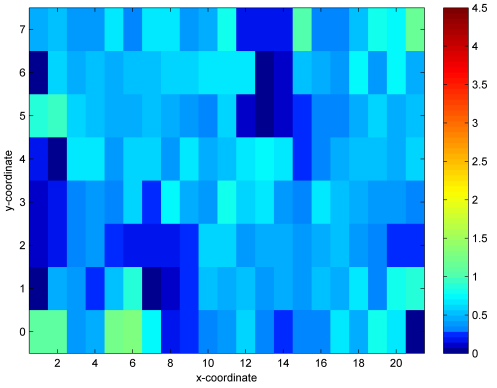


(f) RA II $T_{int2} = 4$ns.

Figure 5.7: LOS-scenario: positioning error color-coded [m]

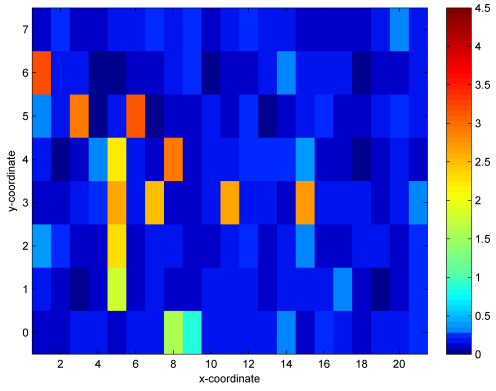


(a) RA I $T_{int2} = 1$ns.

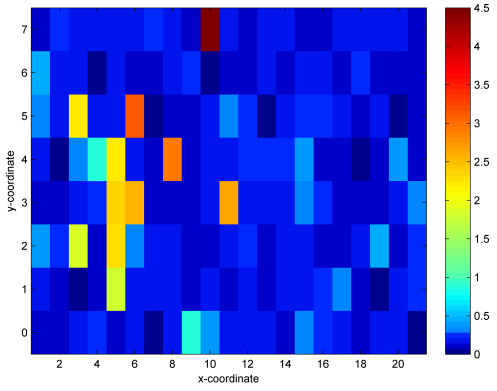


(b) RA II $T_{int2} = 1$ns.

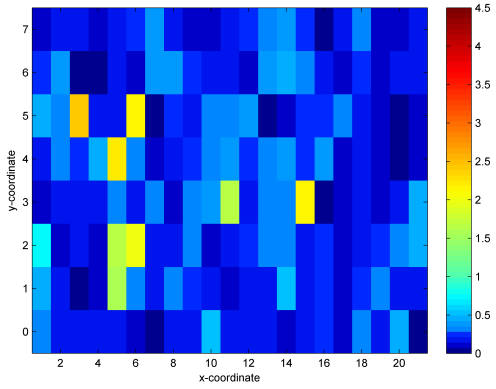


(c) RA I $T_{int2} = 2$ns.

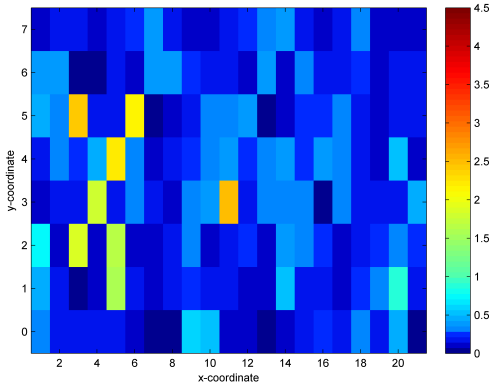


(d) RA II $T_{int2} = 2$ns.

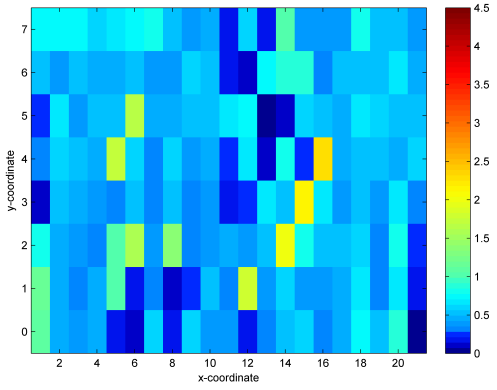


(e) RA I $T_{int2} = 4$ns.

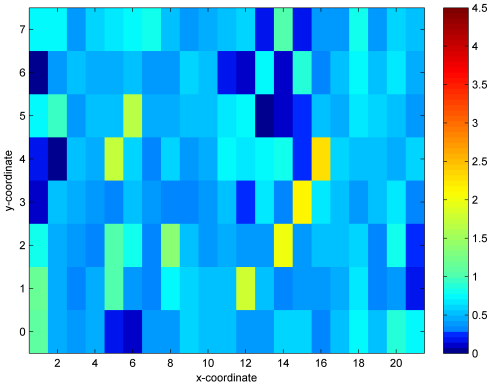


(f) RA II $T_{int2} = 4$ns.

Figure 5.8: NLOS-scenario: positioning error color-coded [m]

### 5.5.1 Error distribution

To investigate the distribution of the positioning error, several fits of different distributions are laid over the histogram of the positioning error in order to find out which distribution fits the best. This is illustrated in Figure 5.9, where among Normal, Rayleigh and Rician distribution, the so-called t location-scale distribution is fitted to the histogram of the positioning error. It seems that the t location-scale distribution fits the best for both the LOS- and NLOS-scenario for all integration times. While the Normal distribution fits well for $T_{int} = \{2, 4\}$ns, it does not converge to the histogram for $T_{int2} = 1$ns. One would expect the error distributions to be symmetrical, but as it shows for short integration times, the histograms have heavier tails (more prone to outliers) than the normal distribution.

One reason for this could be that the space on the left side of the mean is clearly limited by the fact that there is no negative positioning error. Thus more outcomes fall in the small space causing greater density, while on the right side the tail fades to zero more slowly. For longer $T_{int2}$, the mean of the positioning error is shifted to the right and the histogram becomes approximately normally distributed.

Figure 5.10 shows the positioning error histograms for LOS- and NLOS-scenario for integrations times $T_{int2} = \{1, 2, 4\}$ns and the corresponding t location-scale fits.

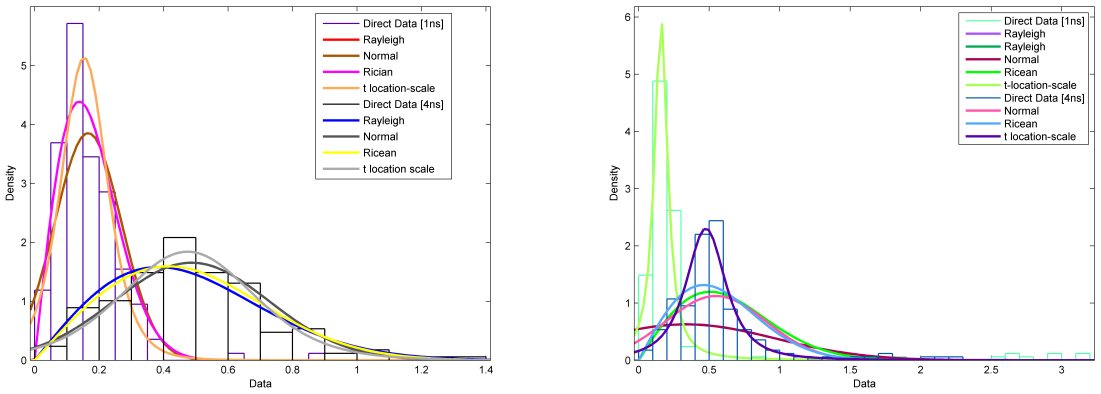


(a) LOS-scenario (b) NLOS-scenario

Figure 5.9: Distribution fits for positioning error histogram (RAI).

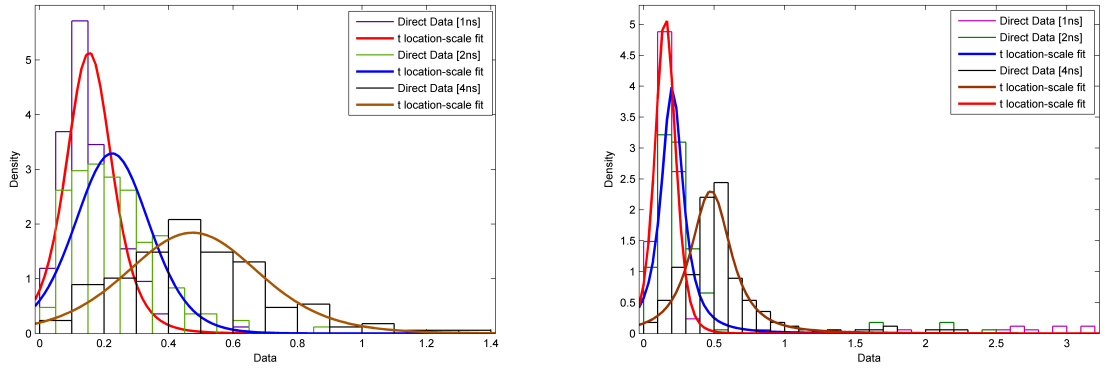


(a) LOS-scenario: RA I (b) NLOS-scenario: RA I

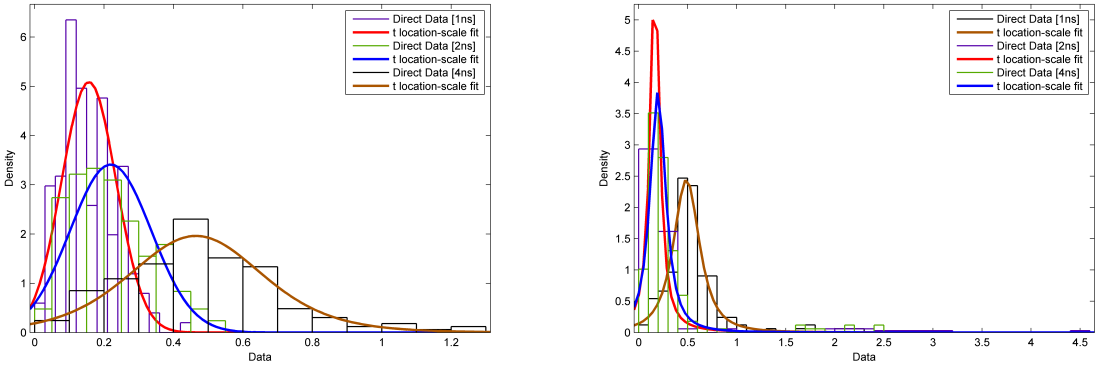


(c) LOS-scenario: RA II (d) NLOS-scenario: RA II

Figure 5.10: t location-scale fits for positioning error histograms.

## 5.6 GUI

The user interface is implemented in MATLAB using the GUI layout editor. It is designed to visualize the result of the positioning process, the OTD-hyperbolas, the borders of the room, the position of the BSs, as well as the impulse responses, and the SNR. A choice can be made between RAI, RAII and positioning using ranging markers from the preprocessing. The latter has the advantage that a high processing gain can be achieved by using the combined symbols from SYNC and SFD as ranging markers. The user triggers the DSO acquisition process by pressing the button for positioning. The data is fetched from the scope, then preprocessed followed by positioning, and finally the result is illustrated. The GUI is illustrated in 5.11.

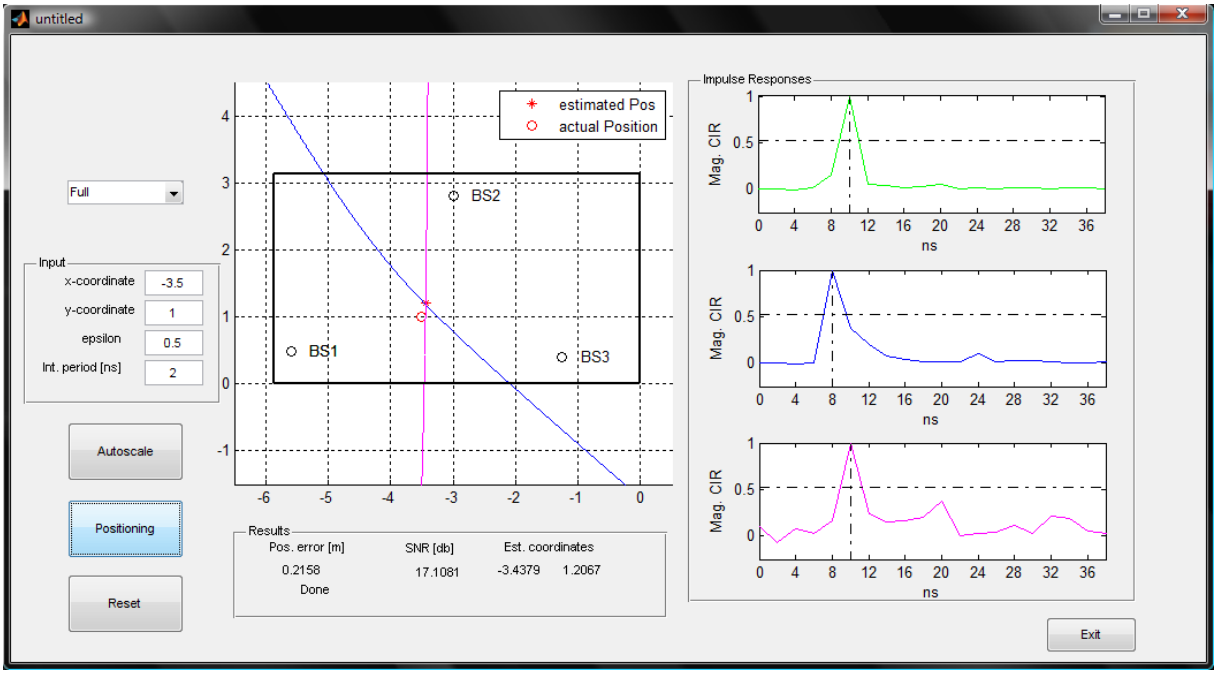


Figure 5.11: The graphical user interface showing positioning results.

# Chapter 6

# Conclusions and Outlook

In this thesis a step by step approach from signal acquisition to positioning using the UWB-IR part of the IEEE 802.15.4a standard is presented. The approach relies on the energy detector, a non-coherent receiver architecture that is well known for its low-complexity, and threshold-based detection and ranging algorithms to perform time-based localization of a mobile.

The problem of signal acquisition has been adressed by calculating thresholds with the help of hypothesis testing. The acquisition process was analyzed concerning the degrading effects that come as a trade-off when reducing complexity and the results have been discussed. Two ranging algorithms have been presented and compared to each other with the help of numerical simulations in their ranging accuracy, robustness and mathematical complexity. The latter has been analyzed on a high-level abstraction by calculating the total number of operations each ranging algorithm needs to process the incoming signal. The crucial and challenging topic of finding the correct TOA of the signal - the LOS-component - has been done by the use of a searchback algorithm.

Subsequently, the theoretical work has been put to a test by practical evaluation. A tracking system has been set up and the developed ranging algorithms have been tested with the UWB demonstrator system [Buc08] in pseudo real time. A GUI has been implemented that serves as a positioning extension for the demonstrator. It gives the user input options and provides feedback information such as the estimated position of the mobile and the channel IRs.

Finally, the result of the measurement setup has been put into graphs and discussed. The ranging performance has been shown to be slightly better for RA I at low SNR in terms of robustness, but its mathematical complexity is significantly higher than that of the second proposed algorithm. The overall results fulfill the aim of the IEEE 802.15.4a

task group of providing sub-meter accuracy in both positioning and ranging.

Since the system works without synchronization, only the difference in signal delays of different BSs is known to the receiver. Therefore the TDOA technique has been used for positioning, leaving the TOA approach open as a topic of further investigation. Furthermore, the influence of the geometric setup of a tracking system has not been looked at very closely.

Another topic of future investigation is the use of different values for preamble parameters $L$ and $N_{code}$, since those have been fixed throughout this entire work as well, as the pulse duration $T_p$, which can be shortened to up to 0.74ns in order to lower the possible spatial resolution to approximately 0.2m. Other leading edge detection techniques, especially for NLOS-scenarios, would also be an interesting topic in this context.

# Appendix A

# Symbols

| | |
|---|---|
| $\delta_i[n]$ | Delta function of length $i$ |
| $\mathbf{A}_i$ | SFD symbols |
| $\mathbf{C}_i$ | Ternary code |
| $\mathbf{M}_i$ | Spread SFD symbols |
| $\mathbf{N}_i$ | Spread SYNC symbols |
| $\mathbf{S}_i$ | Spread ternary code |
| $\mathcal{N}(\mu, \sigma^2)$ | Normal distribution with mean $\mu$ and variance $\sigma^2$ |
| $\Phi[k]$ | Autocorrelation function |
| $h_c(t)$ | Channel impulse response |
| $L$ | Spreading length |
| $n(t)$ | Noise term |
| $N_c$ | Number of chips per symbol |
| $N_{code}$ | Length of ternary sequence |
| $N_{sfd}$ | Number of SFD symbols |
| $N_{snyc}$ | Number of SYNC symbols |
| $p(t)$ | UWB pulse |
| $P(x, \mathcal{H}_i)$ | Probability of $x$ when $\mathcal{H}_i$ is true |
| $p_i(t)$ | Wave form during SYNC portion |
| $T(x)$ | Test statistics on x |
| $T_{int}$ | Integration time |
| $T_{psym}$ | Preamble symbol duration |
| $T_{sfd}$ | Duration of SFD part |
| $T_{sync}$ | Duration of SYNC portion |
| $x_i(t)$ | Composed SHR waveform |

$z_i(t)$ ..... Wave form during SFD
$T_c$ ..... Chip duration
$T_p$ ..... Pulse duration
PRF ..... Peak pulse repetition frequency

# Appendix B

# Measurement Setup

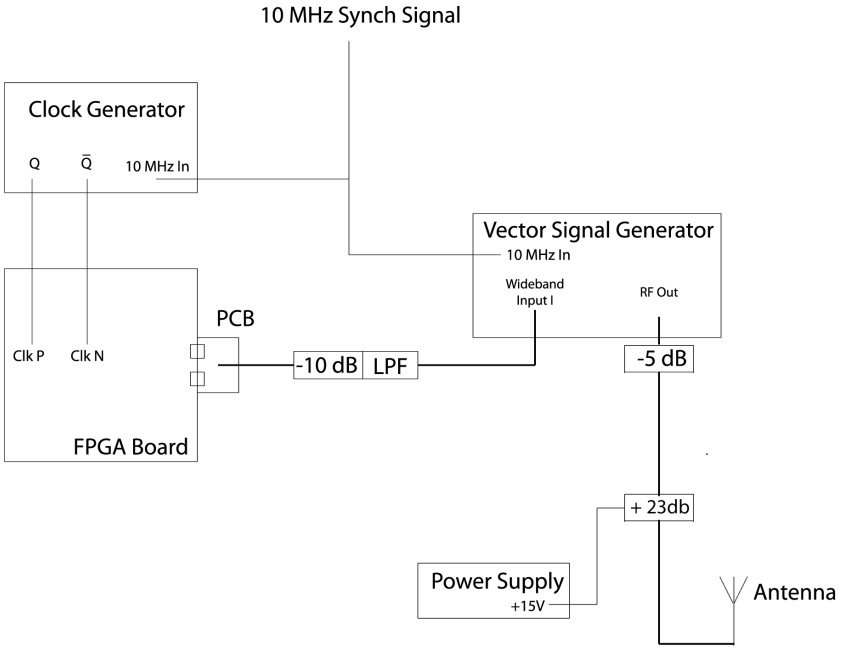


Figure B.1: TX setup

## B.1 TX Setup

The signal is generated by the IEEE 802.15.4a demonstrator system [Buc08], which is a field-programmable gate array (FPGA), timed by a clock generator set to 125MHz with output set to 3.3V (CMOS). The FPGA delivers positive and negative pulses that are combined in a directly connected printed circuit board (PCB). From there on the pulses are fed into a 10dB attenuator. Pulse shaping is done by an adjacent low-pass filter in

| | TX | BS1 | BS2 | BS3 |
|---|---|---|---|---|
| Antenna | 5 Cent | 2 Cent | Skycross | 5 Cent |
| Filter | - | minicircuits | minicircuits | Epcos |
| Amplifier | Miteq 1445755 | Narda 0208N315 | Narda 0208N315 | Miteq |
| Cable | B 5m/S2/S3 | B1 2m/S1 2m | B2 2m/G1 2m | B 20m/G2 2m |
| Channel | - | 2 | 3 | 4 |

Table B.1: TX/RX setup for positioning measurements.

order to obtain an IEEE 802.15.4a conform pulse form.

Upconversion is done by a vector signal generator (VSG), which together with the FPGA board is connected to the digital sampling oscilloscope (DSO), because the DSO serves as master for synchronization purposes by providing a 10MHz reference time base. This reference base is needed in order to achieve synchronization between pulse generation and upconversion and to ensure that sampling on receiver side is also performed synchronously. The VSG output amplitude is set to -20.5dBm, the frequency to 4.5GHz. After upconversion, the signal is attenuated by an Agilent attenuator set to -5dB before it is amplified by a 23dB power amplifier. The attenuator is installed for fine adjustments in context with the calibration, because transmit power on the VSG can only be changed in 5dBm steps.

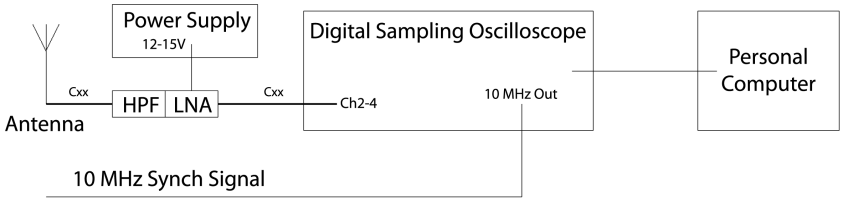


Figure B.2: RX setup.

## B.2 RX Setup

On the receiver side three antennas are connected to a high-pass filter (HPF) and a low-noise amplifier (LNA), before connected to separate input channels of the DSO, where the signal is digitized. The cables used to connect to the DSO are named Bx for the blue, Gx for the green, and B for the black one. The x stands for an additional identifier. The cables with their specific length, as well as LNAs and HPF are listed in Table B.1.

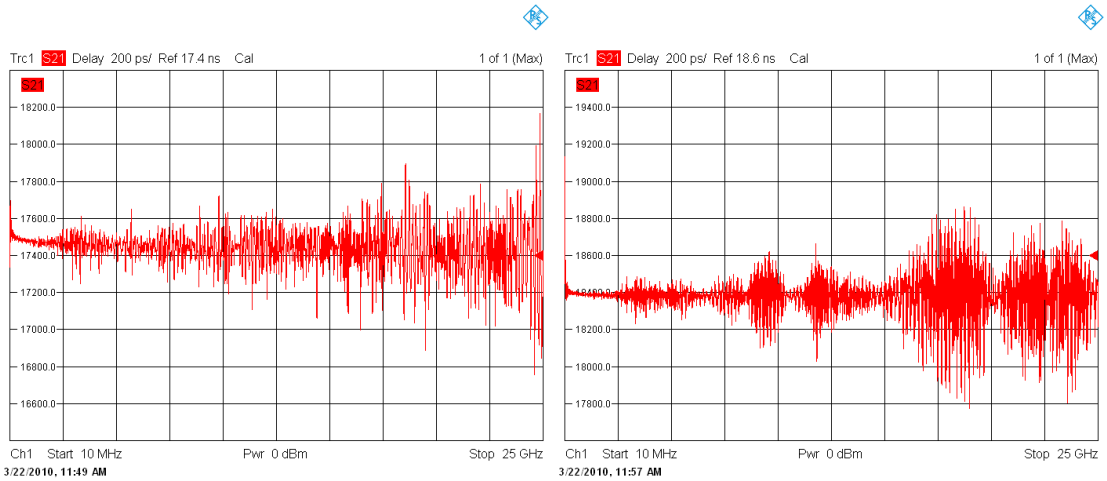


(a) Total delay BS1-DSO.

(b) Total delay BS2-DSO.

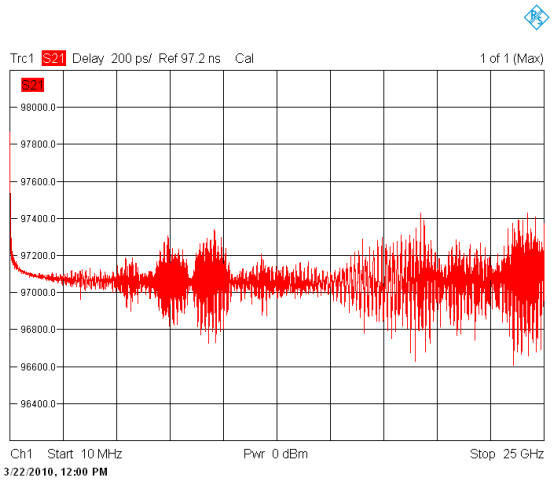


(c) Total delay BS2-DSO.

Figure B.3: Total delays caused by the composite cables.

In order to get correct OTD, additional delays caused by different cable lengths are taken into account. The delays and frequency profiles are measured by the help of a signal network analyzer (SNA) and the results are depicted in Figure B.4. The composite signal path delays from the BSs to the DSO are depicted in Figure B.3, where in addition to the particular blue cable a second cable of length 2m is used to connect the antenna with the LNA and filter.

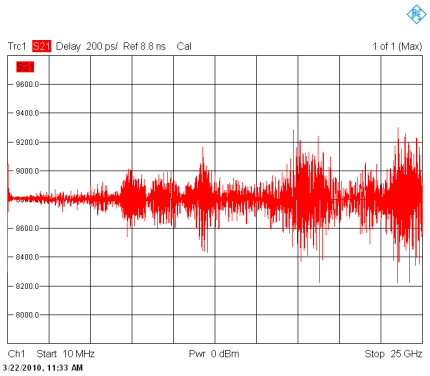


(a) Blue cable 1 (B1 2m) delay.

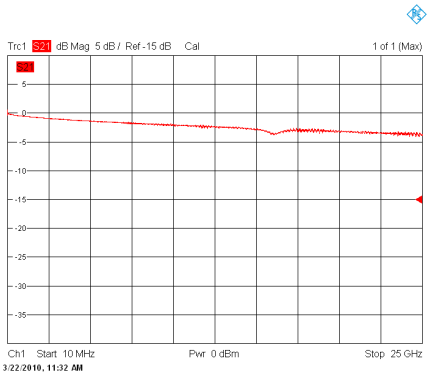


(b) B1 2m frequency profile.

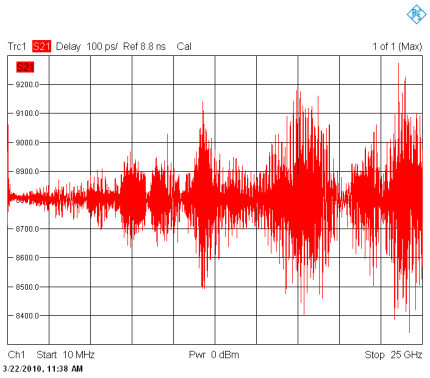


(c) Blue cable 2 (B2 2m) delay.

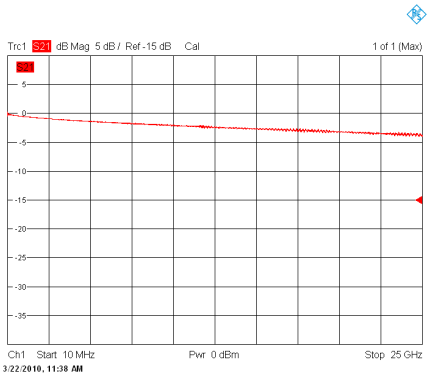


(d) B2 2m frequency profile.

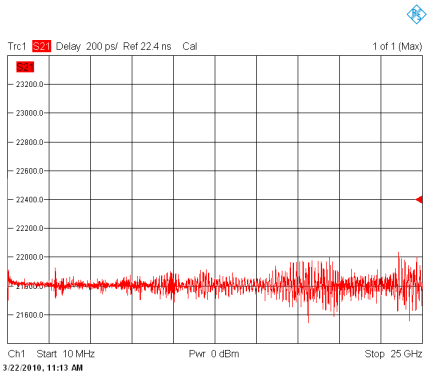


(e) Blue cable (B 5m) delay.

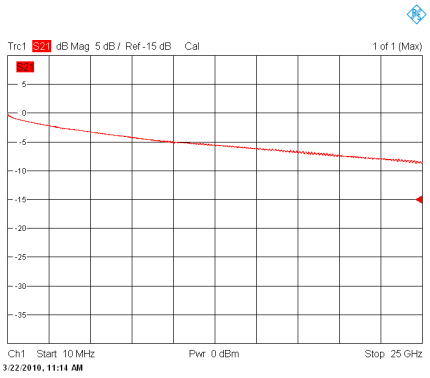


(f) B 5m frequency profile.

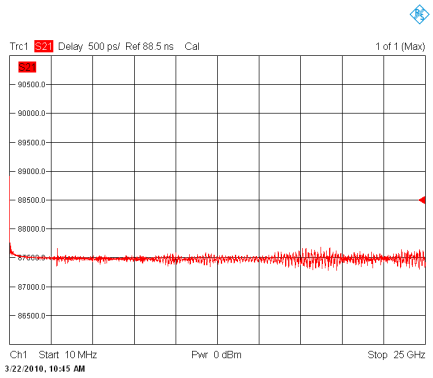


(g) Blue cable (B 20m) delay.

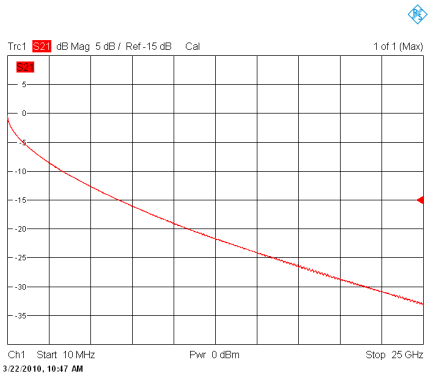


(h) B 20m frequency profile.

Figure B.4: Delay and frequency profiles of the used cables.

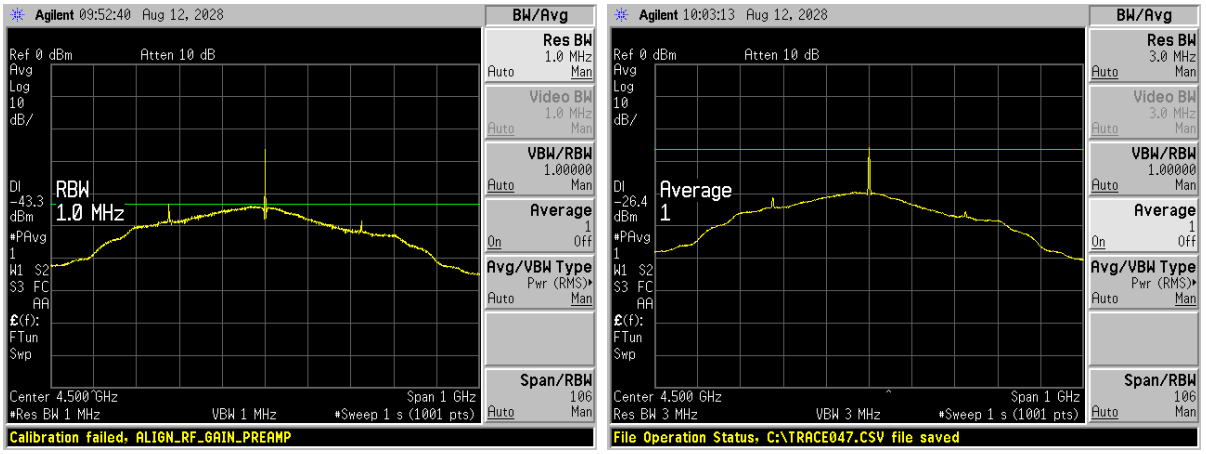


(a) Average EIRP (b) Peak EIRP

Figure B.5: Calibration Measurements

## B.3 Calibration

The FCC regulations for the transmission of UWB define an average power and a peak power limit. The average power limit is set so that the EIRP (Equivalent isotropically radiated power) density averaged over 1ms for a bandwidth of 1MHz lies below -41.3dBm. The demonstrator system is set to $N_{sync} = 64$, $N_{sfd} = 64$, $L = 16$, $N_{code} = 31$, and the counter stop value which initiates the retransmission of the frame is set to 12500, resulting in 5 frames sent during a period of 1ms. With a longer intermission between frames, a higher amplitude could be used, but this is not done due to the fact that the duration of fetching the signal from DSO to PC is intended to be as short as possible. The gain of the used antenna is about 2dBi and taking this into account, the averaged EIRP has to be less than -43.3dBm.

The peak power limit has to be below 0dBm for a center frequency of 4.5GHz. The limit for the peak EIRP for a resolution bandwidth (RBW) smaller than 50MHz can be calculated according to Equation (B.1).

$$-2 - 20 \log \frac{50}{RBW} \tag{B.1}$$

With RBW = 3MHz the peak power limit has to be set to -26.43dBm

With the attenuator in the TX-path set to 5dB this results in an amplitude parameter of -20.5dBm that needs to be set in the VSG user interface. Figure B.5 shows the results of the calibration.

## B.4 Measurement Grid

The grid is set up like illustrated in Figure 5.5 from Chapter 5. Please note that the illustration is not true to scale. The grid has a resolution of 21×8 measurement points and is spaced 0.1m, resulting in 168 measurement points where the corresponding files are named in the following way:

`ch2_x0_y0.mat`

The first three letters identify the channel of the DSO and thereby the BS where the signal is received. The x, y value specifies the location within the grid, beginning with $(0, 0)$ for the origin. The files are saved in directories named "LOS" and "NLOS" depending on the scenario they come from. For the NLOS scenario BS1 is blocked by (the author's) human head.

## B.5 Photographs

In the following two pictures the measurement setup in the HF-laboratory is photographed from different angles. For better illustration, the BSs and the TX are circled by a white and a red marker, respectively.


Figure B.6: The measurement setup in the HF-Laboratory(1).


Figure B.7: The measurement setup in the HF-Laboratory (2).

# Bibliography


[Aic06] Oswin Aichholzer. Entwurf & Analyse von Algorithmen. Lecture notes, Institut für Softwaretechnologie, Graz University of Technology, 2005/06.

[Buc08] Thomas Buchgraber. Experimental Evaluation of the IEEE 802.15.4a Standard. Master's thesis, Signal Processing and Speech Communication Laboratory, Graz University of Technology, Austria, 2008.

[Cea05] F. Chin and et. al. Impulse radio signalings for communication and ranging. *IEEE 802.15.4a standard doc. no. 15-05-0231-07-004a*, July 2005.

[DDdRO05] S. Dubouloz, B. Denis, S. de Rivaz, and L. Ouvry. Performance analysis of LDR UWB non-coherent receivers in multipath environments. In *Ultra-Wideband, 2005. ICU 2005. 2005 IEEE International Conference on*, page 6 pp., Sept. 2005.

[DMT09] A.A. D'Amico, U. Mengali, and L. Taponecco. Ranging algorithm for the IEEE 802.15.4a standard. In *Ultra-Wideband, 2009. ICUWB 2009. IEEE International Conference on*, pages 285 –289, Sept. 2009.

[GBG+09] Thomas Gigl, Thomas Buchgraber, Bernhard Geiger, Ayse Adalan, Josef Preishuber-Pfluegl, and Klaus Witrisal. Pathloss and delay-spread analysis of multipath intensive environments using IEEE 802.15.4a UWB signals. In *9th COST2100 Management Committee Meeting*, TD(09)965, Vienna, Austria, Sept. 2009.

[Gei09a] B. Geiger. Ranging in the IEEE 802.15.4a standard using energy detectors. In *EUROCON 2009, EUROCON '09. IEEE*, pages 1956 –1963, May 2009.

[Gei09b] Bernhard Geiger. Enhanced Accuracy Channel Estimation (and Ranging) Using Energy Detectors. Master's thesis, Signal Processing and Speech Communication Laboratory, Graz University of Technology, Austria, 2009.

[GG03] F. Gustafsson and F. Gunnarsson. Positioning using time-difference of arrival measurements. In *Acoustics, Speech, and Signal Processing, 2003. Proceedings. (ICASSP '03). 2003 IEEE International Conference on*, volume 6, pages VI – 553–6 vol.6, April 2003.

[Gig06] Thomas Gigl. UWB Indoor Positioning based on Recieved Signal Strength. Master's thesis, Signal Processing and Speech Communication Laboratory, Graz University of Technology, Austria, 2006.

[GPPAW09] Thomas Gigl, Josef Preishuber-Pfluegl, Daniel Arnitz, and Klaus Witrisal. Experimental characterization of ranging in IEEE802.15.4a using a coherent reference receiver. *IEEE Intern. Symp. on Personal, Indoor, and Mobile Radio Communications, PIMRC, Tokyo, Japan*, Sept. 2009.

[GTG+05] S. Gezici, Zhi Tian, G.B. Giannakis, H. Kobayashi, A.F. Molisch, H.V. Poor, and Z. Sahinoglu. Localization via ultra-wideband radios: a look at positioning aspects for future sensor networks. *Signal Processing Magazine, IEEE*, 22(4):70 – 84, July 2005.

[IEE07] IEEE standard for information technology - telecommunications and information exchange between systems - local and metropolitan area networks - specific requirement part 15.4: Wireless medium access control (MAC) and physical layer (PHY) specifications for low-rate wireless personal area networks (WPANs). *IEEE Std 802.15.4a-2007 (Amendment to IEEE Std 802.15.4-2006)*, pages 1 –203, 2007.

[Kay93] Steven M. Kay. *Fundamentals of Statistical Signal Processing - Detection Therory.* Prentice Hall Signal Processing Series. Prentice Hall PTR, 1993.

[Mau09] Rainer Mautz. Overview of current indoor positioning systems. *Geodesy and Cartography*, pages 18 – 22, 2009.

[SG06] Z. Sahinoglu and S. Gezici. Ranging in the IEEE 802.15.4a standard. In *Wireless and Microwave Technology Conference, 2006. WAMICON '06. IEEE Annual*, pages 1 –5, Dec. 2006.

[SM98] M.A. Spirito and A.G. Mattioli. On the hyperbolic positioning of GSM mobile stations. pages 173 –177, Sept. 1998.

[Urk67] H. Urkowitz. Energy detection of unknown deterministic signals. *Proceedings of the IEEE*, 55(4):523 – 531, April 1967.

[WLJ+09] Klaus Witrisal, Geert Leus, Gerald J. M. Janssen, Marco Pausini, Florian Trösch, Thomas Zasowski, and Jac Romme. Noncoherent ultra-wideband systems: An overview of recent research activities. *IEEE Signal Processing Magazine*, July 2009.